Publications   Physics and Astronomy

8-1-2010

Locating the Accretion Footprint on a Herbig Ae Star: MWC 480

C A. Grady
Eureka Scientific

K Hamaguchi
University of Maryland

G Schneider
University of Arizona

B Stecklum
Thuringer Landessternwarte Tautenburg

B E. Woodgate
NASA Goddard Space Flight Center

See next page for additional authors

Authors

C A. Grady, K Hamaguchi, G Schneider, B Stecklum, B E. Woodgate, J E. McCleary, G M. Williger, M L. Sitko, F Menard, Th. Henning, and Sean D. Brittain

LOCATING THE ACCRETION FOOTPRINT ON A HERBIG Ae STAR: MWC 480

C. A. GRADY[1,2], K. HAMAGUCHI[3,4,5], G. SCHNEIDER[6], B. STECKLUM[7], B. E. WOODGATE[8], J. E. MCCLEARY[9],
G. M. WILLIGER[10,11,12], M. L. SITKO[13,14,28], F. MÉNARD[15], TH. HENNING[16], S. BRITTAIN[17], M. TROUTMANN[17], B. DONEHEW[17],
D. HINES[13], J. P. WISNIEWSKI[18,29], D. K. LYNCH[19,28], R. W. RUSSELL[19,28], R. J. RUDY[19,28], A. N. DAY[14], A. SHENOY[20],
D. WILNER[21], M. SILVERSTONE[1], J.-C. BOURET[22,23], H. MEUSINGER[7], M. CLAMPIN[8], S. KIM[6], R. PETRE[24], M. SAHU[25],
M. ENDRES[26,27], AND K. A. COLLINS[10,30]

[1] Eureka Scientific, 2452 Delmer, Suite 100, Oakland, CA 96002, USA
[2] ExoPlanets and Stellar Astrophysics Laboratory, Code 667, Goddard Space Flight Center, Greenbelt, MD 20771, USA
[3] CRESST and X-ray Astrophysics Laboratory, NASA/GSFC, Greenbelt, MD 20771, USA
[4] Department of Physics, University of Maryland, Baltimore County, 1000 Hilltop Circle, Baltimore, MD 21250, USA
[5] Goddard Center for Astrobiology, NASA's Goddard Space Flight Center, Greenbelt, MD 20771, USA
[6] Steward Observatory, The University of Arizona, Tucson, AZ 85721, USA
[7] Thüringer Landessternwarte Tautenburg, Sternwarte 5, D-07778 Tautenburg, Germany
[8] ExoPlanets and Stellar Astrophysics Laboratory, NASA's Goddard Space Flight Center, Greenbelt, MD 20771, USA
[9] Department of Astronomy, New Mexico State University, Las Cruces, NM 88003, USA
[10] Department of Physics, University of Louisville, Louisville, KY 40292, USA
[11] Department of Physics and Astronomy, John Hopkins University, Baltimore, MD 21218-2686, USA
[12] Laboratoire Fizeau, Université de Nice, UMR 6525, 06108 Nice Cedex 2, France
[13] Space Science Institute, 4750 Walnut St., Suite 205, Boulder, CO 80301, USA
[14] Department of Physics, University of Cincinnati, Cincinnati, OH 45221-0011, USA
[15] Laboratoire d'Astrophysique de Grenoble, CNRS/UJF UMR 5571, France
[16] Max-Planck-Institut für Astronomie, Königstuhl 17, D-69117 Heidelberg, Germany
[17] Department of Physics and Astronomy, Clemson University, Clemson, SC 29634-0978, USA
[18] Department of Astronomy, University of Washington, Box 351580, Seattle, WA 98195, USA; jwisnie@u.washington.edu
[19] The Aerospace Corporation, Los Angeles, CA 90009, USA
[20] NASA Goddard Space Flight Center, Summer High School Intern and Thomas Wootton High School, Rockville, MD 20850-3099, USA
[21] Harvard-Smithsonian Center for Astrophysics, MS 42, 60 Garden St., Cambridge, MA 02138, USA
[22] Laboratory for Observational Cosmology, Code 665, NASA's Goddard Space Flight Center, Greenbelt, MD 20771, USA
[23] Laboratoire d'Astrophyique de Marseille, CNRS-Université de Provence, Traverse du Siphon-BP8, F-13376 Marseille Cedex 12, France
[24] X-Ray Astrophysics Laboratory, NASA's Goddard Space Flight Center, Greenbelt, MD 20771, USA
[25] United States Patent and Trademark Office, Alexandria, VA 22314, USA
[26] Wyle Information Systems, McLean, VA 22102, USA
[27] Endres' Gamebit Ltd., SE5 7HS London, UK

ABSTRACT

Accretion is a fundamental process which establishes the dynamics of the protoplanetary disk and the final properties of the forming star. In solar-type stars, the star–disk coupling is determined by the magnetic field structure, which is responsible for funneling material from the disk midplane to higher latitudes on the star. Here, we use pan-chromatic data for the Herbig Ae star MWC 480 to address whether similar processes occur in intermediate-mass stars. MWC 480 has X-ray emission typical of actively accreting Herbig Ae stars, but with $\sim 10\times$ more photoelectric absorption than expected from optical and FUV data. We consider three sources for the absorption: the disk, absorption in a wind or jet, and accretion. While we detect the disk in scattered light in a re-analysis of archival *Hubble Space Telescope* data, the data are consistent with grazing illumination of the dust disk. We find that MWC 480's disk is stratified, geometrically thin, and is not responsible for the observed photoelectric absorption. MWC 480 drives a bipolar jet, but with a mass-loss rate that is low compared to other Herbig Ae stars, where the outflow is more favorably oriented and enhanced photoelectric absorption is not seen. This excludes a jet or wind origin for the enhanced photoelectric absorption. We compare MWC 480's O VI emission with other Herbig Ae stars. The distribution of the emission in inclination, and lack of a correlation of profile shape and system inclination excludes equatorially confined accretion for the *FUSE* Herbig Ae stars. The photoelectric absorption data further suggest that the accretion footprint on MWC 480 and other Herbig Ae stars is located at high-temperate, rather than polar, latitudes. These findings support the presence of funneled accretion in MWC 480 and Herbig Ae stars, strengthening the parallel to T Tauri stars.

Key words: ISM: jets and outflows – protoplanetary disks – stars: individual (MWC 480) – ultraviolet: stars – X-rays: stars

Online-only material: color figure

1. INTRODUCTION

Herbig Ae stars are the higher mass analogs of classical T Tauri stars, and resemble them both in their circumstellar disk properties and in the presence of accretion-related phenomena. Recent studies also suggest that they have magnetic fields

---

(Alecian et al. 2008; Hubrig et al. 2009; Wade et al. 2007, 2009). For T Tauri stars, the magnetic field and its geometry affect how and where the disk couples to the star and are thought to be crucial in launching bipolar outflows. The presence of kilo-Gauss magnetic fields in T Tauri stars has permitted tomographic studies of the magnetic field geometry and mapping of the accretion footprint, with indications that the field components and latitude of the accretion footprint on the star differ with the mass of the protostar (Donati et al. 2008, 2010). In other cases, long-duration X-ray observations, spanning the stellar rotation period, have been used to constrain the footprint location (e.g., DG Tau A; Güdel et al. 2007; Grosso et al. 2007) to high latitude. In addition to mapping the location of the X-ray-emitting regions, photoelectric absorption by gas in these same accretion funnels is thought to produce the depressed X-ray fluxes of classical T Tauri stars compared to weak-line T Tauri stars (Gregory et al. 2007).

Herbig Ae stars are also X-ray sources (Hamaguchi et al. 2005; Swartz et al. 2005; Skinner et al. 2004; Stelzer et al. 2009; Günther & Schmitt 2009; Testa et al. 2008; Telleschi et al. 2007), although lacking the hard, flaring, coronal component typical of T Tauri stars. Together with a several orders of magnitude drop in L_X at the end of accretion (Stelzer et al. 2006), the data for early to mid-A Herbig Ae stars suggest that, absent low-mass stellar companions, X-ray emission is produced in the accretion shock, and thus should be near the accretion footprint on the stellar photosphere. Constraining the location of the X-ray-emitting region on a Herbig Ae star can allow us to establish the extent to which the accreting plasma is channeled by the stellar magnetic field, as seen for classical T Tauri stars. However, mapping the latitude range of the X-ray-emitting plasma on pre-Main Sequence (PMS) stars requires knowledge of the viewing geometry, in tandem with good measures of extinction and measured gas absorption columns toward the star. For intermediate-mass stars, constraints on the viewing geometry can be provided either by millimeter interferometry or by high-contrast coronagraphic imaging, while gas absorption columns are best established for lightly reddened, comparatively nearby stars with FUV spectra.

One such star with imagery of the disk, X-ray data, and FUV spectroscopy is MWC 480 (HD 31648, A3psh3+, $B = 7.90$, $V = 7.73$, $J = 6.865$, $H = 6.262$, $d = 131 \pm 20$ pc (van den Ancker et al. 1998); PM = [6.25, −23.8] ± [1.29, 0.81] mas yr⁻¹). MWC 480 is an older (7 Myr; Simon et al. 2000), $1.65 \pm 0.07\,M_\odot$, single, Herbig Ae star which was the first to be imaged at millimeter wavelengths (Mannings et al. 1997), and which has subsequently been the object of detailed disk chemistry studies (Simon et al. 2000; Piétu et al. 2007). The star has also been extensively spectroscopically studied in the IR (Meeus et al. 2001; Sitko et al. 2008), optical (Kozlova et al. 2007; Beskrovnaya & Pogodin 2004), and in the UV (Sitko et al. 1981). Blondel & Tjin A Djie (2006) fit MWC 480 as $R_* = 1.67\,R_\odot$, and adopt $L_* = 11.2\,L_\odot$ from van den Ancker et al. (1998).

Recent, pan-chromatic studies of PMS stars have demonstrated the potential to view the disk and star as a system, and to provide insight into the larger-scale environment of the disk and star. X-ray data allow us to not only measure L_X and the spectrum of the star, but are sensitive to absorption by gas and dust grains up to 10 μm in size, providing a probe of material in the line of sight to the star and, for favorable inclinations, through the disk (K. Arraki et al. 2010, in preparation). FUV spectra for Herbig Ae stars are dominated by emission from the accretion shock,

and from lines associated both with accreting material and in some cases stellar activity. Absorption in transitions of H_2 and $H\,\textsc{i}$ seen against this emission spectrum constrains the gas column toward the emission-line region. The circumstellar disk can most directly be probed at longer wavelengths. Coronagraphic imagery traces where dust in the disk can scatter light from the star, constraining the size, inclination, and vertical geometry of the dust disk. In tandem with gas data, such imagery can probe whether gas and dust in the disk are well-mixed, as well as providing critical data needed to constrain models of the disk based on the IR spectral energy distribution (SED). For disks with well-established inclinations, we can establish whether the line-of-sight gas and dust measures are dominated by absorption or extinction within the disk exterior to the dust sublimation radius, are restricted to regions interior to the dust sublimation radius, or are dominated by more distant, foreground material. Optical narrow-band imagery can establish the presence, spatial extent, and geometry of mass loss via a stellar jet. Such pan-chromatic studies provide a more comprehensive view of the disk and star than is available through single-technique or wavelength observations. We present such a pan-chromatic investigation of MWC 480 to test the hypothesis that the latitude range for the accretion footprint onto MWC 480, and other Herbig Ae stars, is similar to that of classical T Tauri stars.

2. OBSERVATIONS AND DATA REDUCTION

As part of our pan-chromatic investigation, we present new *Chandra* X-ray data, *Far Ultraviolet Spectrographic Explorer (FUSE)* data, optical Goddard Fabry–Perot (GFP) and narrow-band imagery, and optical through mid-IR spectroscopy of MWC 480, together with a re-analysis of archival *Hubble Space Telescope (HST)* coronagraphic imagery of the star. Table 1 lists the mixture of data available for MWC 480, together with the goals of the observations.

2.1. Chandra ACIS-S

MWC 480 was observed by the *Chandra X-Ray Observatory* on 2008 April 7 for 9.8 ks (sequence ID: 200520, under program 09200730, Grady, PI) using the Advanced CCD Imaging Spectrometer (ACIS; Garmire et al. 2003). To ensure the highest soft energy response, MWC 480 was placed at the ACIS-S aim point, and data were obtained using the default 8″.3 × 50″.6 field of view (FOV). When used as an imager in this configuration, ACIS-S provides imagery with FWHM = 0″.5 and pulse height spectra from 0.4 to 8.0 keV.

The data were analyzed using the CIAO[31] software package ver. 4.1. A cross-correlation between the Two Micron All Sky Survey (2MASS) catalog and the ACIS-S data yielded four sources in common within 220″ of MWC 480's nominal position, with a mean offset between the 2MASS frame and the ACIS data of −0″.39 in declination, consistent with the pointing accuracy of *Chandra*. Figure 1(a) shows the central 5′ × 5′ ACIS field.

X-ray events were extracted within 2″ of MWC 480. This radius includes more than 95% of the total point source flux. The background, measured in an annulus about MWC 480 with 20″ outer and 4″.46 inner radii was 5.0×10^{-3} counts arcsec⁻² in 9.8 ks with no evidence for any localized enhancements. As a result, we did not subtract background. No significant light variation was observed during the 3.33 hr integration. We

---

[31] http://cxc.harvard.edu/ciao/

Table 1
Observational Data for MWC 480

Observation	Type	Goals
Chandra X-ray imaging	New	L_X, presence of accretion, photoelectric absorption
FUSE FUV spectroscopy	New	Accretion diagnostics (excess light, emission lines) $N(H_2)$ absorption
UV spectroscopy	Archival	Accretion diagnostics (Lyα emission), N(H I)
GFP coronagraphic imagery	New	Jet presence and extent
TLS narrow band imagery	New	Jet extent, proper motion, inclination
Optical spectroscopy	New	Jet radial velocity, inclination
HST coronagraphic imagery	Archival	Dust disk structure, outer radius, inclination
NIR photometry	Both	IR light variation and correlation with imagery
NIR spectroscopy	New	IR light variation, accretion diagnostics
Phoenix Mid-IR spectroscopy	New	Molecular gas dynamics, inclination dependence
Mid-IR spectroscopy	Both	IR light variation and correlation with imagery

generated response matrices and auxiliary files using `acisspec`. MWC 480 was detected, but was unexpectedly faint, yielding only 150 counts. The spectrum shows a low energy cutoff, suggesting significant soft X-ray absorption. Above 0.7 keV, the X-ray spectrum is typical of accreting Herbig Ae stars such as HD 163296 (Swartz et al. 2005; Günther & Schmitt 2009), but at a lower flux. We fit the spectrum binned with 20 photon counts bin^{-1} by an absorbed 1 T thin-thermal plasma (wabs*apec) model with the elemental abundances fixed at 0.3 solar. The plasma temperature and hydrogen column were 0.47 (0.29–0.60) keV and 5.2 (3.3–7.2) $\times$ 10^{21} cm^{-2}, respectively, with a reduced $\chi^2 = 1.77$ for degrees of freedom (dof) = 5. The spectrum is shown in Figure 1.

2.1.1. Chandra ACA Photometry

In addition to the X-ray telescope, *Chandra* is equipped with the Aspect Camera Assembly (ACA) which is used in target identification and tracking, and can be used for broadband optical photometry. MWC 480 itself was not used as a guide star, since there were suitable guide stars farther from the intersection of the aspect camera CCD chip boundaries at the center of the FOV. However, MWC 480 was used as an optical acquisition star to confirm spacecraft attitude, and was tracked for a few readouts immediately before the X-ray observation. The aspect camera recorded the target with an aspect camera magnitude of 8.0, which can be converted to more conventional filter photometry using the relation[32]

$$m_{aca} = V + 0.426 – 1.06(B-V) + 0.617(B-V)^2 – 0.307(B-V)^3$$

from the *Chandra* Proposers' Observatory Guide. Using the $B-V$ color listed on SIMBAD, the star was at $V \sim 7.76$ at the time of the ACIS-S observation, consistent with both the photometry of Beskrovnaya & Pogodin (2004) and the value tabulated on SIMBAD.[33]

2.2. FUSE FUV Spectra

MWC 480 was observed three times in 2004, on March 5 (D0650101), October 22 (D0650102), and October 24 (E5100101), by *FUSE* using the $30'' \times 30''$ LWRS aperture under GI programs D065 and E510. *FUSE* consisted of four co-aligned spectroscopic channels with independent telescopes, reflection gratings, and choice of entrance aperture (Moos et al. 2000). The spectral data were processed with the CALFUSE 3.0.7 pipeline (Dixon et al. 2007), and subsequently handled as described in Collins et al. (2009). Table 2 lists the effective exposure times in each of the spectroscopic channels for each of the *FUSE* observations. Data for segments SiC2A and SiC2B for D0650101 were excluded due to anomalously high background.

MWC 480 has a faint continuum which can be traced from 1000–1186 Å, together with emission in C III (977 Å (marginal detection) and 1176 Å), O VI (1032 Å and 1038 Å), as well as faint Fe II emission near 1120 Å, and the expected airglow lines due to *FUSE*'s low-Earth orbit (Figure 2(a)). The continuum is detected in all three observations, with no significant variation. After co-adding the mean continuum flux at 1160 Å is $\sim 9 \times 10^{-14}$ erg cm^{-2} s^{-1} Å^{-1}, consistent with the deepest of the short wavelength *International Ultraviolet Explorer* (*IUE*) observations, SWP 43428. The Fe II emission shows no significant variation from observation to observation.

Minor variation from observation to observation is found for the C III lines, while the O VI doublet varies by a factor of 2 in flux (Figure 2(b)). Superposed on the O VI emission is absorption from H_2 (Figure 2(c)), as is typical of Herbig Ae spectra (Martin-Zaïdi et al. 2008). To better characterize the timescale of variation in 2004 October, we measured the O VI 1032 flux for each orbit of observations D0650102 and E5100101, which covers a span of 2.3 days. The signal-to-noise ratio (S/N) for any individual orbit is 0.6–1.5 per 0.013 Å (3.8 km s^{-1} at 1032 Å) pixel^{-1}. We calculated feature significance using the 1σ error arrays output by CALFUSE for LiF1A, which was by far the highest signal channel segment. Given that the signal was insufficient to model the line profiles well, we simply summed the flux in the emission line, without correcting for H_2 absorption or subtracting off any continuum or background. The continuum and background were very low in any case, making the integration bounds (which varied slightly from orbit to orbit) very easy to identify by eye. We examined errors in two ways. First, we used the error array output by CALFUSE to calculate the error in the summed flux. Second, we made three measurements of each line, taking the widest, optimal, and narrowest integration bounds which we considered reasonable. The standard deviation of the three measurements was comparable to the calculated error for any one measurement. We adopted the standard deviation for our error bars. The emission line was detected in all orbits, suggesting that any flux dropouts due to MWC 480 wandering out the LWRS aperture

---

[32] See Section 5.8.3 of the *Chandra* Proposers' Observatory Guide at http://cxc.harvard.edu/proposers/POG
[33] See the *Chandra* Proposer's Observatory Guide, prepared by the *Chandra* X-ray Center, and the *Chandra* Project Science, MSFC, and IPI teams: http://cxc.harvard.edu/proposer/POG/html/index.html.
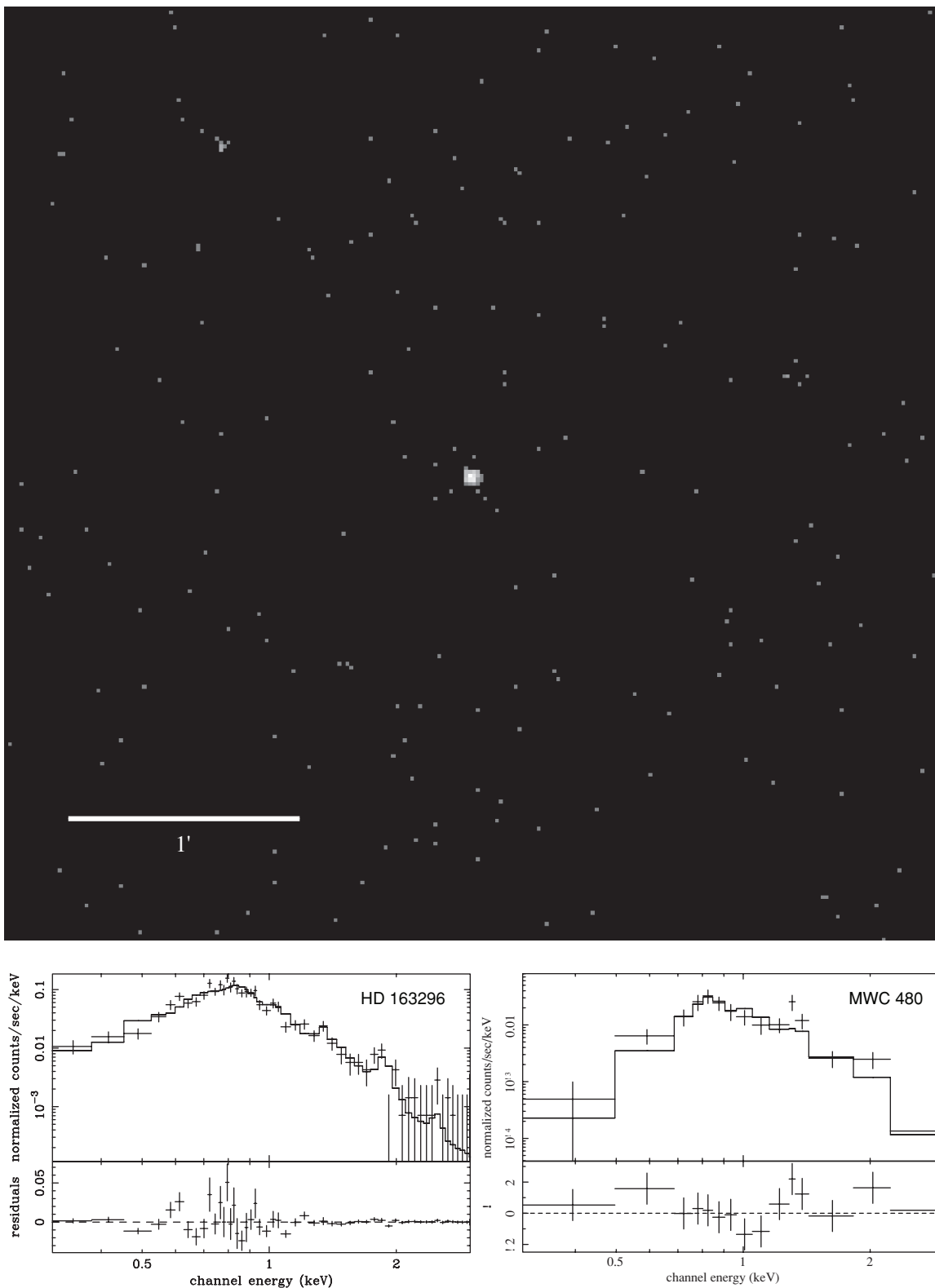
Figure 1. MWC 480 in the X-ray: upper: *Chandra* ACIS-S field for MWC 480 showing only one other X-ray source lies within a field ±2 arcmin centered on MWC 480. Lower: comparison of X-ray spectra for HD 163296 (after Günther & Schmitt 2009) and MWC 480. Compared to HD 163296, MWC 480 has a soft X-ray deficit, but a similar X-ray spectrum (modulo S/N) above 0.7 keV.

during the orbits were small. Inspection of the O VI 1032 Å data binned over the emission line and plotted as a function of time reveals a trend of decreasing flux through the two observations, and marginally significant variation within the observations (Figure 2(d)).

2.3. HST Coronagraphic Imagery

MWC 480 has been coronagraphically observed three times by *HST* (Table 3) with non-detections previously reported for NICMOS F160W imagery (observation id = N4N03010,
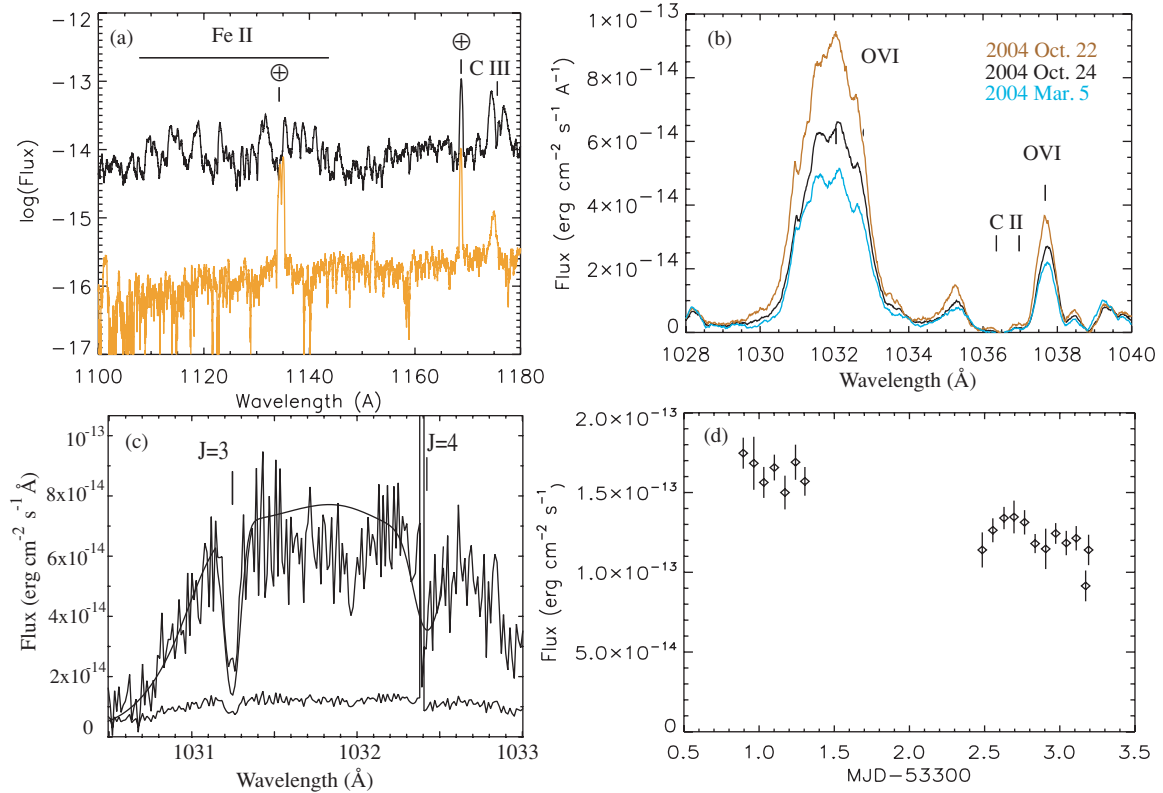
Figure 2. MWC 480 in the FUV. (a) MWC 480 exhibits excess continuum light, in addition to an emission-line spectrum when compared to main-sequence early to mid-A stars scaled to the V magnitude of the star. Here β Pictoris is shown as a comparison star (gold). (b) MWC 480 has variable O $_{VI}$ emission, here shown for the three FUSE spectra, smoothed by a 31 point boxcar filter to suppress noise and make the faint continuum more clearly visible. From observation to observation, MWC 480 varied by a factor of 2 in O $_{VI}$ during 2004. (c) Superposed on the O $_{VI}$ and C $_{II}$ profiles, MWC 480 has H_2 absorption, shown here for the ($\nu = 0$, $J = 3$) and ($\nu = 0$, $J = 4$) transitions (see Martin-Zaïdi et al. 2008), as seen in the 2004 October 24 spectrum. (d) When the individual orbits of the 2004 October observations are plotted, there is an overall decrease in O $_{VI}$ 1032 emission strength, with a marginal detection of variability.

Table 2
Integration Times for *FUSE* Spectral Observations

ID	T_{exp}/N_{exp}							
	L1A	L1B	L2A	L2B	S1A	S1B	S2A	S2B
D0650101	12945/11	9186/6	11059/8	9946/7	8768/7	2936/4	$\cdots$	$\cdots$
D0650102	18672/7	18852/7	16644/7	17569/7	18672/7	18852/7	16644/7	17569/7
E5100101	27315/8	29253/9	26363/9	27118/9	28446/9	29253/9	26363/9	27118/9

$\lambda_{eff} = 1.6\,\mu m$, obtained on 1998 February 24; Augereau et al. 2001) and *HST*/STIS($\lambda_{eff} = 0.58\,\mu m$, 2000 February 4 (O5KQ170) and 2000 February (5O5KQ180); Grady et al. 2005). These observations were supplemented by NICMOS F110W observation from 2004 November 21 (N8ZU23IFQ, N8ZU24IHQ). The NICMOS F110W data were obtained prior to an *HST* secondary mirror movement, with point-spread function (PSF) data obtained following the mirror motion, precluding subtraction of contemporary PSF template data and will not be further discussed.

2.3.1. NICMOS 1.6 μm

NICMOS coronagraphic images of MWC 480 obtained on 1998 February 24 (HST-GO-7857, A.-M. Lagrange, PI) were re-reduced, calibrated, and processed following the methods described in Schneider et al. (2005). Eleven SAMP-SEQ = STEP8, NSAMP = 10 (39.95 s integration) multiaccum exposures using the F160W filter were obtained with the target centered behind the coronagraphic obscuration. The star was observed at only one spacecraft orientation. A second star, HD 29646 ($H - K = 0.021$), was contemporaneously observed, intended in the original program to be used as a PSF subtraction template.

Detection of a disk in scattered light typically relies not just on the obscuration of the central star, but depends critically upon subtraction of a template PSF observation to remove the bulk of the stellar diffracted and instrumentally scattered light (Grady et al. 2007). For NICMOS, the practice has been to make use of observations of PSF template stars that are as bright or brighter than the science target to ensure similar exposure of the wings of the PSF with data taken within the same *HST* cycle to ensure that the optical elements of the NICMOS coronagraph have similar alignment in the dewar, and that the *HST* focus is similar. The NICMOS filters most frequently used for coronagraphic imagery have 25% bandpasses, which can result in significant PSF shape differences between the science target and PSF template, unless both stars are close in $J - H$ or $H - K$. Such color effects are particularly important if the disk is faint in scattered light. Optimally, the science target and

Table 3
Journal of *HST* Coronagraphic Observations

Date	Inst.	ID	λ_{eff} (μm)	T_{exp} (s)	Prog.	Ref.
			MWC 480			
1998 Feb 24	NIC2	N4NL03010	1.6	439.5,895	7857	Augereau et al. (2001)
2000 Feb 4	STIS	O5KQ170	0.58	1680	8474	Grady et al. (2005)
2000 Feb 5	STIS	O5KQ180	0.58	1680	8474	Grady et al. (2005)
2004 Nov 21	NIC2	N8ZU23IFQ	1.1	224	10177	This study
		N8ZU24IHQ	1.1	224	10177	This study
			MWC 758			
2000 Jan 16	STIS	o5kq03010	0.58	840	8474	Grady et al. (2005)
2000 Jan 19	STIS	o5kq04010	0.58	840	8474	Grady et al. (2005)

the PSF template observation star should have $|J - H|$ and $|H - K| < 0.3$. MWC 480 ($J - H = 0.603$, $H - K = 0.735$) is redder in the NIR than any unreddened main-sequence star, and significantly redder than HD 29646, thus accounting for the non-detection reported by Augereau et al. (2001). Fortunately, NICMOS observed a number of main-sequence M stars in *HST* cycle 7 as part of program HST-GTO-7227. Four of the 34 M stars in this program are as bright or brighter than MWC480 in the F160W band, enabling them to be candidate PSF templates: GL 693, GL 905, GL 445, and GL 729. As PSF subtraction templates for MWC 480, three are disqualified. GL 729 is in a dense stellar field, GL 445, is ill-matched in *HST* focus or "breathing" phase, and a differential "cold mask shift" in the GL 905 data with respect to MWC 480 is substantial. The remaining star, GL 693 ($H = 6.297$, $J - H = 0.558$, $H - K = 0.28$), appears well matched in breathing phase and cold mask location, and was observed in two visits at different spacecraft roll (celestial orientation) angles.

An estimate of the MWC 480/GL 693 photospheric flux density ratio in F160W was derived from the corongraphic data by adjusting the intensity in the GL 693 subtracted image to simultaneously null (bring to zero) the flux density of the PSF-subtracted images (treating the two visits, V59 and V60, separately) and minimize the variance in the region beyond where any disk flux contribution is seen. The region chosen for minimizing the variance was empirically selected to be $1\farcs5 \leqslant r \leqslant 3\farcs$. We found that the scale factor applied to the GL 693 data to best null the underlying stellar PSF of MWC 480 was 0.860. Both subtractions show mid-spatial frequency residuals due to color mismatches, and due to changes in *HST* focus, especially the "eleven-thirty finger" and a zonal undersubtraction at $r \sim 13$ pixels ($0\farcs975$), which is worse in the GL693 Visit 60 images. These systematics, and to a lesser extent the uncertainty in the flux scaling, limit the efficacy of absolute photometric measures derived from these images.

The 1σ uncertainty in the MWC 480:PSF flux scaling by this method is $\leqslant 2\%$. To understand the resulting uncertainty in the derived radial profiles, images made with under/ oversubtractions deviating by this amount in PSF scaling (scale factors of 0.88 and 0.84) were created and radial profiles were measured. However, the effects while measurable do not dominate over the uncertainties resulting from the higher spatial frequency residuals arising from breathing and color effects. The two independent PSF-subtracted images were median combined and the result is shown oriented on the sky in Figure 3(a). A fit to the azimuthally averaged radial surface brightness profile is shown in Figure 3(b).

2.3.2. STIS Coronagraphic Imagery

MWC 480 was observed with Space Telescope Imaging Spectrograph's (STIS's) coronagraphic imaging mode ($\lambda_{\text{eff}} = 5875$ Å, but including $0.2 - 1.0 \, \mu$m) on 2000 February 4 (observation id = o5kq18010) and almost 22 hr later on 2000 February 5 (observation id = o5kq17010) as part of HST-GTO-8474 (Grady et al. 2005). The disk was not detected after subtraction of PSF template images that were poor color matches, but detailed comparison of the roll-differenced data shows features that are not seen in similar data (Figure 4) for the mid-A Herbig Ae star HD 36112 (MWC 758, $V = 8.29$, $B - V = 0.25$ id = o5kq03010, o5kq04010). The first, a linear nebulosity along P.A. = 237°, is accompanied by a lower surface brightness *feature* along P.A. = 57°. These features are along the disk semi-minor axis (Simon et al. 2000; Piétu et al. 2007). Faint centro-symmetric features are also present in the roll-differenced imagery, but are sufficiently complex and in a region where differences in the dispersed speckles can be large, precluding further analysis. The linear nebulosity is more clearly shown in difference-sum imagery (Figure 5) which obscures features within $2''$ of the star.

2.4. Goddard Fabry–Perot Narrow-band Imaging

MWC 480 was observed with the GFP Interferometer at the Apache Point Observatory 3.5 m telescope on 2005 December 30 and 2006 February 27. The observations were made using two etalons, providing resolutions of $120 \, \text{km s}^{-1}$ and $600 \, \text{km s}^{-1}$, respectively. MWC 480 was occulted by a coronagraphic wedge for all observations (Table 4). The instrument, the use of the coronagraphic wedge to facilitate detection of jets associated with Herbig Ae stars, and data reduction for the jet imagery are described in Wassell et al. (2006). At Hα, nebulosity is detected along P.A. = 57°/237° (Figure 6(a)).

2.5. Optical Long-slit Spectroscopy

A confirming long-slit optical spectrum of MWC 480 with the slit aligned along P.A. = 57° was obtained on 2007 February 11 at the Apache Point Observatory 3.5 m telescope using the DIS (see description in Grady et al. 2007). MWC 480 was observed with a $1\farcs2$ slit and imperfectly centered under a $2''$ wide occulting bar. The spectrum covers 6340–7450 Å with a resolution of $50 \, \text{km s}^{-1}$. The slit covers a region $\pm 2\farcs5$ from the star with sampling of $0\farcs4$ per pixel. Seeing was $\approx 0\farcs8$–$1\farcs0$ during the observation, with cirrus. A portion of the red spectrum is shown in Figure 6(b).
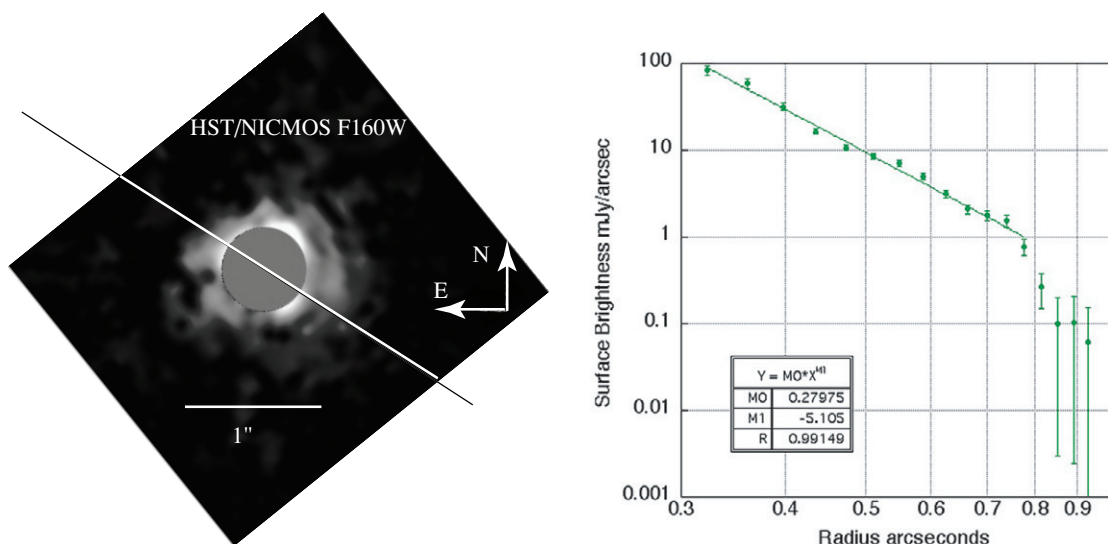
Figure 3. *HST* NICMOS coronagraphic imagery of MWC 480 following PSF subtraction. Left: circumstellar nebulosity is revealed within $1''$ of MWC 480 when the 1998 observation originally discussed in Augereau et al. (2001) is PSF subtracted using a contemporary observation which is a better color match to the star in the NIR. The line indicates the position of the disk semi-minor axis (Piétu et al. 2007). The data are shown with a linear stretch from -2 to 2 ADU s^{-1} pixel^{-1}. The circular region centered on the star represents the $r = 0''.3$ coronagraphic obscuration. Right: the azimuthally averaged radial surface brightness profile for MWC 480 from the 1998 data.

(A color version of this figure is available in the online journal.)
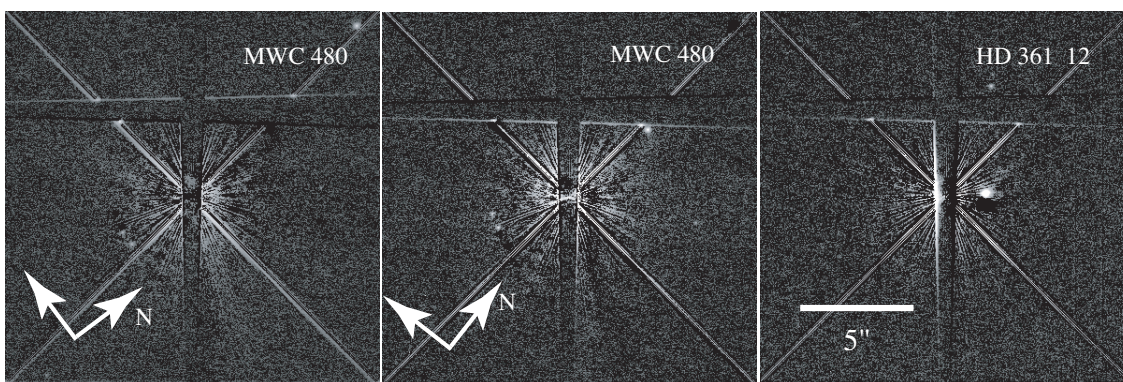
Figure 4. Broadband optical coronagraphic imagery for MWC 480 and HD 36112 (MWC 758): left: roll-differenced imagery (2000 February 4–2000 February 5) for MWC 480 showing an absence of point sources closer than $4''$ from the star, as well as faint residuals near the star and along P.A. $= 57°/237°$. Center: roll-differenced data for 2000 February 5–2000 February 4). Right: roll-differenced imagery for HD 36112 showing an absence of residuals near the star other than a background object at $2''$.

Table 4
Journal of GFP Observations

Date	Etalon	Line	RV (km s^{-1})	Comments
2005 Dec 30	Rutgers Broad	S II 6717	-50 ± 60	Jet non-detection
			-150 ± 60	Jet marginally detected
			-250 ± 60	Jet detected
			-350 ± 60	Non-detection
2006 Feb 27	Far-Red	S II,6717	-50 ± 1400	Jet detected, HH#2 marginally detected
		Hα	-50 ± 1400	Counterjet detected, HH#2 detected

2.6. Wide-field Narrow-band Imaging

Wide-field optical imaging of MWC 480 was performed in 2002 January using the 2k×2k SITe CCD at the prime focus of the 2 m telescope of the Thüringer Landessternwarte Tautenburg (the diameter of the Schmidt correction plate is 1.34 m). The broad and narrow-band images (I, Hα, [S II] $\lambda\lambda$6717, 6731) cover an FOV of $\sim$42$'$ × 42$'$ at a pixel scale of 1$''$.235. Two exposures were done per filter with integration times of 180 s, 600 s, and 1200 s, respectively, to enable the reliable removal of cosmic rays. The images were flat fielded with dome flats

and astrometrically calibrated using 10 stars from the DSS2 (POSS–II[34]). Second epoch images in the I and Hα bands were obtained one year later using the same setup and integration times. Adjacent sky regions east and west of MWC 480 were also imaged in I and Hα to increase the field coverage to about 126$'$ × 42$'$. The FWHM of the stellar PSFs in the Hα image is about 2$''$.5. In order to facilitate the detection of weak features

---

[34] The Second Palomar Sky Survey was made by Caltech with funds from NSF, NASA, the National Geographic Society, the Sloan Foundation, the Samuel Oschin Foundation, and the Eastman Kodak Corporation.
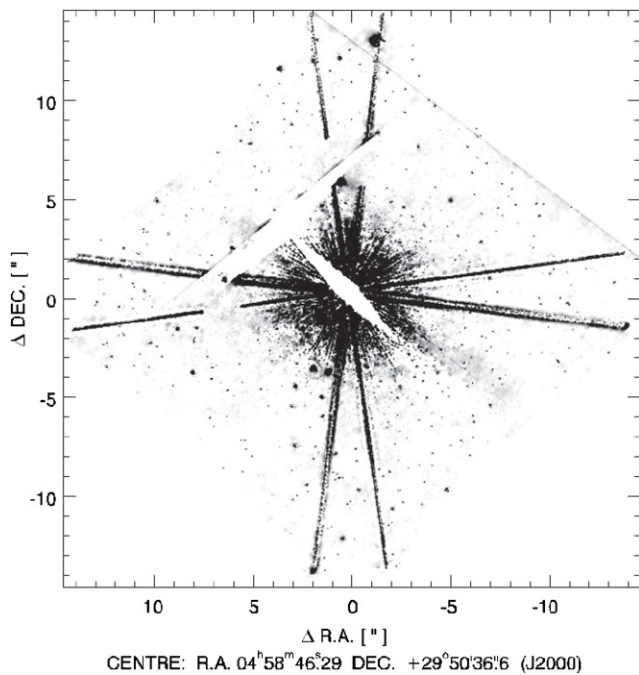
Figure 5. Difference-sum image of the STIS data oriented with N up and E to the left. The nebulosity is along P.A. = 57°/237°.

in the immediate neighborhood of MWC 480 and to minimize the influence of the halo surrounding the bright stars in the continuum subtraction, the azimuthal median in a region of about $140'' \times 140''$ around those stars was subtracted in both the Hα and I images (Figure 7).

2.7. Optical Low-resolution Spectroscopy

To verify the emission-line nature of the features detected in the narrow-band imaging, low-resolution spectroscopy was performed in 2002 February using the Nasmyth spectrograph of the 2 m telescope of the Thüringer Landessternwarte equipped with a 2800×800 pixel SITe CCD. The V200 grism was
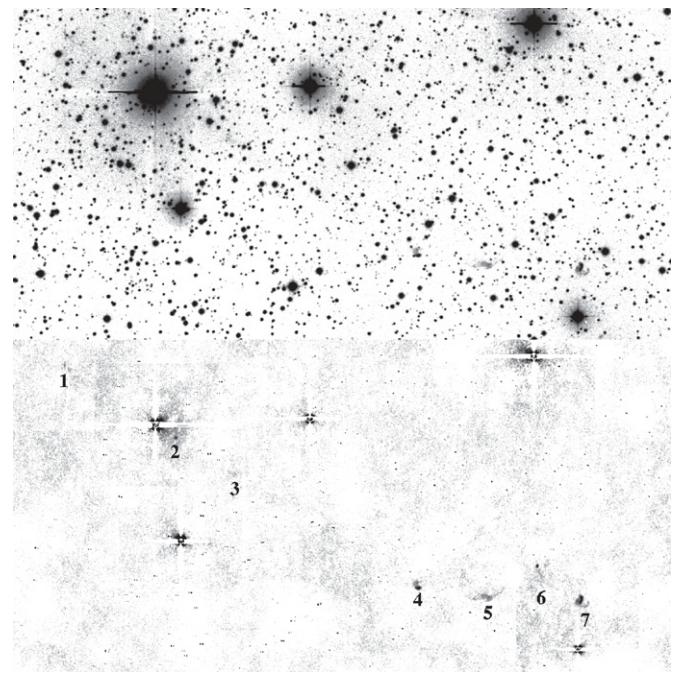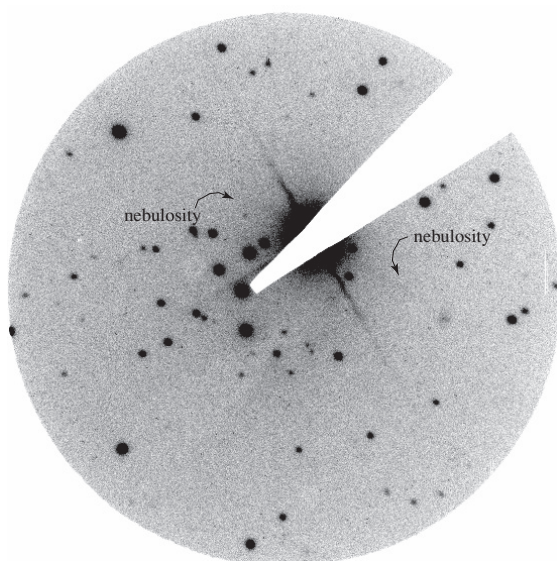

Figure 7. Additional HH knots lie farther from MWC 480, with four knots, including the bowshock seen in the DIS and GFP data, along the disk semi-minor axis, and three more distant knots which are less well aligned with the disk. These objects have been cataloged as HH728. The field in Hα is shown above, and Hα-I band below, suppressing stars and highlighting emission-line nebulosity. The FOV of the Tautenburg Schmidt data is 24.7×12.5.

used, yielding a spectral resolution of $R \sim 600$ and ~ 300 for the selected slit widths of $2''$ and $3''$, respectively. The total integration time per object is 2400 s. Since the atmospheric conditions during these observations were not very good, additional spectroscopy was performed on 2006 March 1. At this occasion, the combination of the V100 grism with a slit width of $1''$ resulted in spectral resolutions of $R \sim 2000$. The wavelength calibration is based on night-sky lines following
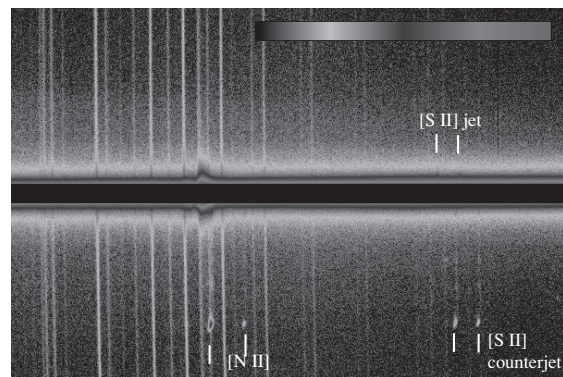

Figure 6. Jet and counterjet of MWC 480: left: GFP coronagraphic imagery in Hα show that the nebulosity seen along the disk semi-minor axis is emission-line nebulosity rather than reflection nebulosity, and extends at least $1'$ from the star. The FOP of the GFP data is 3.75 in diameter. North is up and east to the left in this image. Right: a DIS long-slit spectrum demonstrates that the nebulosity exhibits the S-shaped velocity structure typical of bipolar outflows as well as the low-excitation spectrum typical of HH knots. The brighter jet component is the receding component or counterjet along P.A. = 237°. The FOV shown extends $\pm 92''$ from the star. The region within ± 3.7 of MWC 480 is digitally masked. The positive Y-axis lies along P.A. = 57°, while the negative Y-axis is along P.A. = 237°. The counterjet, which shows substructure, terminates in a bowshock $66'' \pm 4''$ from the star.
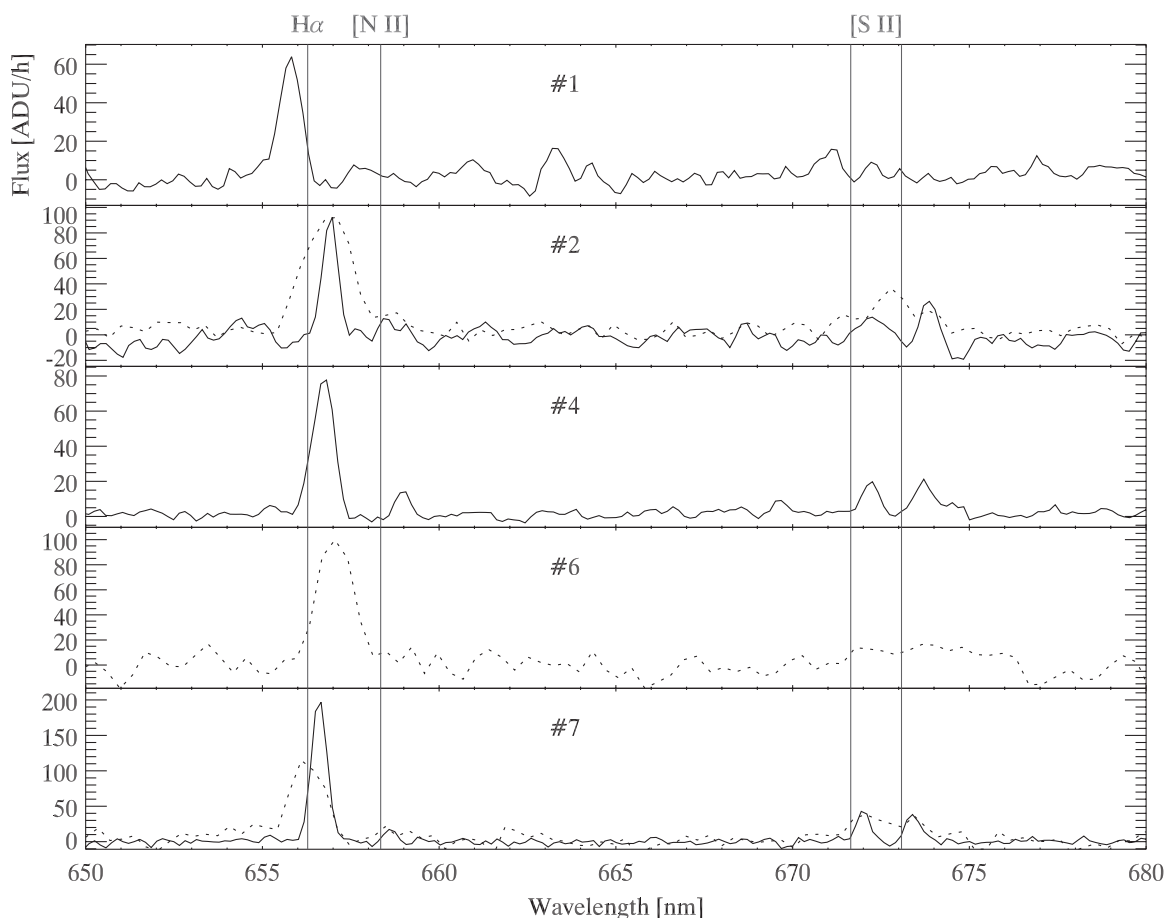
Figure 8. Spectra of the HH 728 knots detected in the Tautenburg Schmidt data, with the same numbering as in Figure 7. Dashed spectra are from 2002, taken with a 2″ slit and $R \sim 500$, while the solid line spectra are from 2006, taken with a 1″ slit at $R = 2000$. HH728-1 is clearly blueshifted, while the other knots are redshifted.

Stecklum et al. (2007). The accuracy of the derived radial velocities is ~ 10 km s^{-1}. Spectra near Hα for the emission line knots identified in Figure 7 are shown in Figure 8.

2.8. Near-IR Photometry

On the same night that spectra of MWC 480 were obtained with SpeX, images in the J, H, and K filters of the SpeX guider camera ("Guidedog") were obtained. This uses the Mauna Kea filter set described by Simons & Tokunaga (2002), Tokunaga et al. (2002), and Tokunaga & Vacca (2005). Three calibration stars were also observed. Two of these, HD 289907 and SA-97-249, are standard stars for the Mauna Kea filter set, and the magnitudes of Leggett et al. (2006) were used. The third was HD 31069, the A0V star used for the spectroscopy, where 2MASS (Skrutskie et al. 2006; Cutri et al. 2003) values were used.

Photometric data in the J, H, K, and L bands were also obtained using the 1.3 m telescope of the Kitt Peak National Observatory. These observations are described more fully by Sitko et al. (2008).

2.9. SpeX 1–5 μm Spectroscopy

MWC 480 was observed as part of a long-duration study of IR SED and accretion diagnostic variability using the SpeX spectrograph at the NASA Infrared Telescope Facility from 2006 through the end of 2009. This study builds on an earlier compilation of IR data from many instruments and facilities which demonstrated significant temporal variation in the IR

SED of MWC 480 (Sitko et al. 2008). The SpeX observations were made using the cross-dispersed echelle gratings in both short-wavelength mode (SXD) covering 0.8–2.4 μm and long-wavelength mode (LXD) covering 2.3–5.4 μm (Rayner et al. 2003). These observations were obtained using a 0″.8 wide slit, corrected for telluric extinction and flux calibrated against the A0V star HD 31069. The data were reduced using the Spextool software (Vacca et al. 2003; Cushing et al. 2004) running under IDL. Due to variable light throughput in the SXD observations of both stars, the overall flux levels were normalized to the LXD observations.

To check for any systematic zero-point shift in the absolute flux scale, we also observed both stars using the low-dispersion prism in SpeX, using a slit that was 3″.0 wide. The stars were observed at air masses of 1.05 (MWC 480) and 1.10 (HD 31069), respectively. To avoid saturation of the detector and minimizing arc line blends, the flat-field and wavelength calibration exposures required a narrower slit, and the 0″.8 slit was used. For clarity, we did not remove the effect of the telluric absorption features from the prism observations. No vertical shifts have been applied to either spectrum, and the two agree to within 5% over the wavelength range in common, suggesting that the echelle spectrum is probably too low by this amount.

2.10. Mid-IR High-resolution Spectroscopy

To represent one of the brightness states of MWC 480, we include spectra obtained with the Short Wavelength Spectrograph of the *Infrared Space Observatory* (*ISO*). These consist

of individual spectral scans in a number of grating orders that require merging. This can introduce uncertainties in the absolute flux levels, particularly where the signal is weak. Here we have used a normalization from 4–7 μm that is slightly lower than that of Sloan et al. (2003), and represents the spectral shape of MWC 480 more reliably, based on comparison with other data sets.

2.11. Mid-IR Medium-resolution Spectrophotometry

MWC 480 was observed with The Aerospace Corporation's Broadband Array Spectrograph System (BASS) on numerous nights between 1996 and 2006 (Sitko et al. 2008). BASS uses a cold beamsplitter to separate the light into two separate wavelength regimes. The short-wavelength beam includes light from 2.9–6 μm, while the long-wavelength beam covers 6–13.5 μm. Each beam is dispersed onto a 58-element Blocked Impurity Band (BIB) linear array, thus allowing for simultaneous coverage of the spectrum from 2.9 to 13.5 μm. The spectral resolution $R = \lambda/\Delta\lambda$ is wavelength dependent, ranging from about 30 to 125 over each of the two wavelength regions (Hackwell et al. 1990).

3. RESULTS

3.1. Modeling of the Chandra CCD-resolution Spectrum and Absence of Close Stellar Companions

Accreting, early to mid-A Herbig Ae stars are routinely detected as X-ray sources with *Chandra*, and MWC 480 is no exception. We had expected that MWC 480 should have an X-ray spectrum resembling that of HD 163296 (Günther & Schmitt 2009), albeit at much lower S/N given our short *Chandra* observation. Above 0.7 keV, this expectation is supported (Figure 1). After correction for absorption, the spectrum corresponds to a source with $kT = 0.47$ (0.29–0.60) keV for the 90% confidence range and with intrinsic $L_X \sim 2 \times 10^{29}$ erg s^{-1}, intermediate between that of HD 163296 (Swartz et al. 2005; Günther & Schmitt 2009) and HD 100546 (Feigelson et al 2003), as expected based on the age of MWC 480 (Simon et al. 2000). The lack of detectable variation in our short ACIS-S integration is also typical of Herbig Ae stars observed with *Chandra*. The temperature of the X-ray spectrum is in general agreement with predictions of the shock model of Calvet & Gullbring (1998) using stellar parameters from Blondel & Tjin A Djie (2006), with a stellar mass of 1.8 $M_\odot$ for MWC 480, or the lower value of 1.65 ± 0.07 $M_\odot$ from Simon et al. (2000).

Our ACIS-S exposure was sufficiently long to marginally detect any wide substellar companions similar to TWA 5B (Tsuboi et al. 2003) or more X-ray luminous objects at S/N ⩾ 2.5. Weak-line T Tauri stellar companions down to M5 would produce ⩾ 100 counts, and would be easily resolved from the Herbig Ae star at $r \geqslant 0\rlap{.}''5$. No such objects are seen. Moreover, such companions would have harder X-ray spectra than observed for MWC 480 (see Collins et al. 2009). Early M stars would dominate the X-ray luminosity of the system: we can exclude late-type companions earlier than M2-M3 at any angular separation from the Herbig Ae primary in this system. The X-ray data are consistent with MWC 480 being a single star with no comoving late-type stellar companions.

3.2. Accretion Rate for MWC 480

It is difficult to measure the accretion rate of Herbig Ae/Be stars in the optical and NIR due to low contrast between the

stellar photosphere and the accretion shock. Muzerolle et al. (1998) showed that the logarithm of the luminosity of Br γ is linearly proportional to the log of the accretion luminosity. Calvet et al. (2004) found a similar, but slightly flatter relationship for intermediate-mass T Tauri stars (the precursors of Herbig Ae/Be stars). While it is tempting to adopt this relationship for Herbig Ae/Be stars, Brittain et al. (2007) summarize several concerns with blindly extrapolating this relationship to earlier spectral type stars. An independent measure of the stellar accretion rate of Herbig Ae/Be stars is the measurement of the veiling of the Balmer discontinuity (Garrison 1978; Muzerolle et al. 2004). The Balmer discontinuity is a sharp decrease in the continuum flux of the stellar photosphere at about 4000 Å, and is particularly prominent for spectral class A and B stars. This sharp decrease is due to the "bunching up" of several absorption lines (mostly hydrogen). Garrison (1978) found that the Balmer discontinuity for Herbig Ae/Be stars is generally less than that found for main-sequence A and B stars. He proposed that the luminosity from mass accretion veils the Balmer discontinuity, causing it to be smaller for Herbig Ae/Be stars. Muzerolle et al. (2004), assuming magneto-accretion, modeled the veiling of the Balmer discontinuity for different accretion rates.

3.2.1. Optical and NIR Estimates of $\dot{M}_{acc}$

Donehew & Brittain (2010) measured the luminosity of Br γ and the mass accretion rate from the veiling of the Balmer break for 36 Herbig Ae/Be stars including MWC 480. They found that for Herbig Ae/Be stars of spectral type A2e and later types these properties followed a trend similar to that presented by Muzerolle et al. (1998) and Calvet et al. (2004):

$$\log(L_{acc}/L_\odot) = (0.77 \pm 0.18)\log(L_{Br\gamma}/L_\odot) + (2.89 \pm 0.61).$$

This is somewhat flatter than the trend found for classical T Tauri stars (slope = 1.26 ± 0.19), but consistent with that found for intermediate-mass T Tauri stars (slope 0.9). Using this relation, they derive mass accretion rates for MWC 480 of 6.6×10^{-8} $M_\odot$ yr^{-1} for their 2006 data and 7.4×10^{-8} $M_\odot$ yr^{-1} for their 2008 data. These rates are a factor of $\approx 2.5 \times$ higher than the accretion rate derived by Blondel & Tjin A Djie (2006) using *IUE* data. From veiling of the Balmer discontinuity, Donehew & Brittain (2010) find $\dot{M}_{acc} = 1.45 \times 10^{-7}$ $M_\odot$ yr^{-1}.

3.2.2. FUV Excess Light

Independent confirmation of on-going accretion can be provided by detection of an FUV or UV excess light continuum. The FUV spectrum of MWC 480 has a faint continuum which drops by a factor of $\sim$3 in flux from 1160 Å down to 1100 Å in all three *FUSE* observations, *much* more gradually than expected for stellar photospheres in the A1–A5V range. In the deepest of the *FUSE* spectra, this continuum can be traced to 1000 Å. We next compared the MWC 480 data to main-sequence standard stars which were scaled to MWC 480's V magnitude and reddened using the Sasseen et al. (2002) extinction law. For A2V (HD 102647, observation id = A0410202000), we expect a flux at 1160 Å of $\sim$4.7 $\times 10^{-16}$ erg cm^{-2} s^{-1} Å^{-1}, *below* the *FUSE* detection limit of 10^{-15} erg cm^{-2} s^{-1} Å^{-1}, and well below the MWC 480's measured flux. The situation is worse for any A3V and A5V stars (Figure 2(a)) in the *FUSE* archive, indicating that MWC 480 has FUV excess light similar to that seen for other, actively accreting Herbig Ae stars.

We can quantify the accretion rate by comparing this excess to other Herbig Ae stars of similar spectral type. The closest match

Table 5
Objects of the HH 728 Herbig–Haro Flow

No.	α_{2000} 04^h	δ_{2000} +29°	d($''$)	$v_{LSR}^{H\alpha}$	$v_{LSR}^{[S\,II]}$	Morphology
1	59 01.9	52 49	123	-267 ± 21	$\cdots$	Diffuse, blend
2	58 42.7	50 07	50	$+255 \pm 10$	$\cdots$	Resolved in GFP, DIS data
3	58 33.5	48 52	190	$\cdots$	$\cdots$	Diffuse
4	58 00.8	44 29	633	$+172 \pm 4$	$+230 \pm 13$	Compact
5	57 49.0	44 08	757	$\cdots$	$\cdots$	Diffuse
6	57 40.2	45 18	810	$+317 \pm 40$	$\cdots$	Compact
7	57 32.7	44 47	921	$+111 \pm 1$	$+114 \pm 3$	Double bow

in spectral type in the *FUSE* archives is to HD 163296. After dereddening the MWC 480 data and scaling to the distance of HD 163296, we find a continuum flux at 1160 Å $\sim 2 \times 10^{-14}$ erg cm^{-2} s^{-1} Å^{-1}, or 44% of HD 163296's flux. HD 163296 has an FUV continuum which has historically varied by a factor of ~ 2 over the ~ 20 years spanned by UV observations. This variability introduces some uncertainty in regards to which continuum level corresponds to the Brγ accretion rate in Garcia Lopez et al. (2006) for HD 163296. However, adopting the Garcia Lopez et al. (2006) accretion rate, we derive $\dot{M}_{acc} \sim 3.8 \times 10^{-8}\, M_\odot$ yr^{-1} for MWC 480. This is within a factor of 2 of the Brγ measurement and is in agreement with the estimate of Blondel & Tjin A Djie (2006).

3.3. MWC 480 Drives a Bipolar Jet

Roll-differenced (Lowrance et al. 1999) STIS coronagraphic imagery revealed nebulosity along P.A. = 57°/237° (Figures 4, 5) consisting of an extended feature to the SW of the star and two knot-like structures to the NE, within 12$''$ of MWC 480. The position angle (P.A.) of the nebulosity coincides with the projection of the disk semi-minor axis (Piétu et al. 2007) on the sky, suggesting that it might be associated with a bipolar jet. The emission-line nature of the feature was confirmed with the GFP imagery, which indicated that the approaching jet component lies along P.A. = 57° while the receding component is along P.A. = 237°. The Dual Imaging Spectrograph (DIS) long-slit spectrum further reveals the S-shaped radial velocity curve expected from a bipolar jet (Figure 6(b)), and shows that the counterjet terminates in a large bowshock, where the flow abruptly decelerates by 200 km s^{-1} over 4$''$.6. The counterjet is brighter in the optical than the jet Herbig–Haro (HH) knots. This asymmetry does not appear to be due to an extinction gradient in the field of MWC 480, but may reflect an outflow asymmetry, similar to that seen for other jet-driving PMS stars. The counterjet termination bowshock is also seen in the wide-field Tautenburg imagery in Hα and [S II] (knot 2), in addition to other, more distant HH knots. The full flow extends over 19$'$ (Figure 7), constituting a parsec-scale outflow. The distant knots (Figure 8) have low-excitation spectra typical of Herbig–Haro Objects (HHOs). Radial velocity data for the knots are listed in Table 5. After correction for $v_{LSR} = 5.1$ km s^{-1} (Mannings et al. 1997), all of the southwestern knots are redshifted relative to the star, while the NE knot is blueshifted, consistent with the jet. The flow is now cataloged as HH 728.

3.3.1. Proper Motion of Knots and Outflow Inclination

HH728 knots 2, 4, 6, and 7 are detected in DSS/DSS2 F plates. The epoch difference of ~ 5 and 46 years between these data and our narrow-band imagery permitted us to investigate their proper motion, although proximity of HH728-2 to

MWC 480 renders the proper motion measurement less certain. HH728-4 is included in the USNOB1.0 catalog (Monet et al 2003, ID 1197-0069101) with an annual proper motion of $\delta_{R.A.} = -274 \pm 40$ mas yr^{-1}, $\delta_{decl.} = -66 \pm 89$ mas yr^{-1}, corresponding to a tangential velocity of 175 ± 37 km s^{-1} at a distance of 131 pc. For this knot we derive an inclination of $45^\circ \pm 6^\circ$ at Hα and $37^\circ \pm 7^\circ$.5 using the S II radial velocity data. Both measurements are consistent at the 1σ level with the disk inclination from the millimeter (Piétu et al. 2007), indicating that the outflow is orthogonal to the disk.

3.3.2. Constraining the Disk Outer Radius in the Optical

The HH 728 counterjet can be traced into 2$''$.2 $\pm$ 0$''$.05 from MWC 480 (Figure 5). Since the counterjet becomes visible when it emerges from behind the protoplanetary disk, this angular distance provides a firm upper limit to the disk size in the optical. For $i = 37^\circ$.5 (Piétu et al. 2007), after deprojection, we derive a disk outer radius $\leqslant 360$ AU, larger than the resolved size of the disk in the millimeter continuum (Piétu et al. 2006), but smaller than the CO disk (Simon et al. 2000; Piétu et al. 2007). However, the apparently large values of the disk outer radius derived in these CO studies may stem from the uncertain nature of the disk surface density distribution of the outer disk, where the simple extrapolation of a single power law is unlikely to apply. As discussed by Hughes et al. (2008), models with the tapered outer edges expected for accretion disks provide a better match to resolved millimeter CO and dust emission data from disks, including MWC 480, due to the steeper fall-off at large radii, far from the star.

3.3.3. Upper Limit to Jet X-ray Luminosity

X-ray emission arising from bipolar jets has previously been reported for classical T Tauri stars (Güdel et al. 2007) and for the Herbig Ae star HD 163296 (Swartz et al. 2005). No extended X-ray emission is detected along the P.A. of the optical jet within 5$''$ of MWC 480. HH 409 A associated with HD 163296 produced 4–6 counts in a 20 ks *Chandra* AIS image. At a distance of MWC 480, this corresponds to 1.8–2.7 counts in our shorter integration, neglecting foreground photoelectric absorption. This is well above the background level seen in the ACIS image, indicating that the luminosity of any X-ray jet from MWC 480 is $\geqslant 2$–3$\times$ *below* that of HD 163296, consistent with the ratio of the accretion luminosities and the optical jet luminosity ratio, despite the different epochs for the accretion data and the coronagraphic imagery.

3.4. Photoelectric Absorption and Extinction Toward MWC 480

The measured photoelectric absorption toward MWC 480 of $N_{X-ray}(H) \sim 5.2 \times 10^{21}$ cm^{-2} corresponds to $E(B - V) = 0.73$
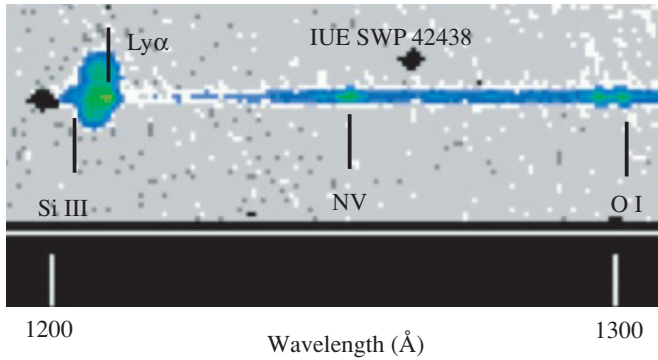
Figure 9. Spectral image of *IUE* SWP 42438 showing point source emission superposed on geocoronal Lyα emission. The presence of this emission indicates that $E(B - V) < 0.08$, and provides a firm upper limit to N(H I) $< 2 \times 10^{20}$ cm^{-2}.

(0.48, 1.05) if produced under conditions typical of the diffuse interstellar medium (ISM; Ryter 1996). Such a large $E(B - V)$ would have observable consequences for the UV and FUV spectrum of the star if produced by foreground material, and would be expected to produce $\Delta A_V = 2.48$ mag if due to material that is transiently in the line of sight. The *Chandra* ACA photometry is consistent with photometry for MWC 480 over the past 2 decades, *excluding* a transient enhancement in the extinction at the time of the X-ray observation. MWC 480 has literature $B - V$ colors ranging from 0.11 to 0.16 (Beskrovnaya & Pogodin 2004) and up to 0.17 as tabulated on SIMBAD. $(B - V)_0 = 0.08$ for A3V, 0.12 for A4V, and 0.15 for A5V, so the measured $B - V$ colors correspond to $E(B - V) = 0.02$–0.09 mag for A3V, -0.01–0.05 mag for A4V, and are too blue for A5V. *International Ultraviolet Explorer* (*IUE*) low-resolution spectra (Sitko et al. 1981) lack the 2175 Å dip which is characteristic of ISM-like extinction curves with $E(B - V) \geqslant 0.25$ mag, providing a firm upper limit to foreground extinction. Further, Herbig Ae stars are faint FUV sources: even $E(B - V) = 0.48$ mag an ISM-like extinction curve (Sasseen et al. 2002) would render a mid-A Herbig Ae star *undetectable* by *FUSE*, in marked disagreement with the successful detection of MWC 480 three times in 2004.

3.5. An Upper Limit to N(H I)

A deep short-wavelength, low-dispersion spectrum of MWC 480, SWP 42438, was obtained on 1991 September 10 during the low radiation portion of the *IUE* orbit, when the spacecraft was farthest from the Earth. The spectrum is saturated longward of 1720 Å, but despite the long exposure duration, is not saturated at H I Lyα (see Figure 9). Superposed on the image of the 10″ × 20″ *IUE* large aperture is circumstellar emission due to MWC 480. The FUV continuum flux near the short wavelength cutoff in *IUE* SWP 42438 is comparable to the continuum flux seen by *FUSE* suggesting that SWP 42438 is representative of MWC 480 in the UV. No high-dispersion UV spectrum covering Lyα with good S/N is available for MWC 480. However, given the presence of a type I P Cygni profile for Mg II in *IUE* LWP 18883 from 1990 September 20, we consider that the intrinsic Lyα profile should closely resemble that of HD 163296 (Devine et al. 2000). For such an emission profile N(H I) $\geqslant 2 \times 10^{20}$ cm^{-2} is sufficient to eliminate all Lyα emission. Given the *IUE* detection of Lyα emission, we find a firm upper bound to N(H I) in the line of sight of N(H I) $\leqslant 2 \times 10^{20}$ cm^{-2}, which we adopt for the remainder of this paper.

Table 6
Molecular Gas Toward MWC 480

Molecule	J	v	log(N)	Error log(N)
H$_2$	0	0	20.0	0.2
	1	0	19.3	0.2
	2	0	19.5	0.2
	3	0	15.5	0.2
	4	0	15.0	0.2
HD	0	0	14.7	0.4

3.6. Molecular Gas In the Line of Sight to MWC 480

Superposed on the O VI emission in the *FUSE* spectra are absorption lines due to H$_2$, similar to that seen in AB Aur (Roberge et al. 2001) and in other Herbig Ae stars (Martin-Zaïdi et al. 2008). These absorption features produce only localized flux deficits against the O VI 1032 Å profile but produce significant absorption in the vicinity of the 1038 Å line. To reconstruct the intrinsic spectrum, we first adopt the observed continuum spectrum. We further note that the variable O VI 1032 Å emission has typically twice the peak flux of the residual emission in 1038 Å, allowing us to assume that the emission is optically thin. We first fit the emission around O VI λ1032, interpolating across the narrow absorption from the $J = 3$ and $J = 4$ lines at 1031.2 and 1032.4 Å, respectively and the HD $J = 0$ line at 1031.9 Å. Next we divided this profile by a factor of 2, and shifted the wavelengths by the O VI doublet ratio to create a synthetic O VI 1038 emission profile. C II 1036.34, 1037.02 Å emission is seen toward some late-A spectral type Herbig Ae stars, but is neglected in our fitting of the MWC 480 data, since we find no residual emission in the vicinity of the lines to allow us to reconstruct the intrinsic spectrum.

We then used VPFIT[35] to fit first the H$_2$ $J = 3, 4$ and HD $J = 0$ profiles at 1031–1032 Å, fixing the radial velocity by $J = 3$ 1031.2 Å and requiring the other lines to be at the same radial velocity. We assumed a Doppler parameter of $b = 7$ km s^{-1} for H$_2$ and $b = 5.7$ km s^{-1} for HD assuming thermal broadening, which are typical empirical values resultant from H$_2$ in the ISM at *FUSE* resolution (e.g., Williger et al. 2005). However, the results are insensitive to the exact Doppler parameters used.

The accuracy of the *FUSE* wavelength scale is discussed in Dixon et al. (2007). For our purposes, it is sufficient to establish a local scale, enabling us to fit the H$_2$ and HD lines consistently. Having established a radial velocity of 17 km s^{-1} from the fits around the O VI 1032 emission line, we then fitted the absorption around O VI 1038, fixing both the radial velocity and Doppler parameter to be the same as for the H$_2$ and HD absorption around 1032 Å. This constrained column densities for the molecular hydrogen lines for $J = 0, 1, 2$ at 1036.6, 1037.2, and 1038.7 Å, respectively. Although the formal errors from the profile fitting are on the order of 0.1–0.2 dex (1σ), we note that uncertainties in the emission profiles and velocity structure render the column densities uncertain by at least a few tenths of a dex, to be conservative. However, the bulk of the absorption is in the $J = 0$ through $J = 2$ levels, resulting in $N(\text{H}_2) \approx 1.4 \times 10^{20}$ cm^{-2}, with trace amounts in the $J = 3$ and 4 levels (Table 6). The total N_{H_2} is similar to that seen toward AB Aur (Roberge et al. 2001) and HD 141569 A (Martin-Zaïdi et al. 2008). Combining $N(\text{H}_2)$ and our limit on N(H I), we find $N_{\text{gas}} = N(\text{H I}) + 2N(\text{H}_2) < 4.8 \pm 0.4 \times 10^{20}$ cm^{-2}. $N_{\text{gas}} \leqslant 0.1* N_{\text{X-ray}}(\text{H})$, but is entirely consistent with $E(B - V)$ toward MWC 480. The molecular

---

[35] www.ast.cam.ac.uk/~rfc/vpfit.html

fraction is >58%, higher than seen toward AB Aur (Roberge et al. 2001), but the ratio $N(HD)/N(H_2)$ is consistent, within the errors, to expectations for the ISM (Snow et al. 2008), favoring a molecular cloud origin for the bulk of the gas seen toward MWC 480.

3.7. The Disk in Scattered Light

We robustly detect the dust disk of MWC 480 at F160W from the 0″3 inner working angle (39 AU) of the NICMOS corona-graph to 0″8 (105 AU; Figure 3(a)). The region over which we detect scattered light from MWC 480's dust disk is both smaller than the size limit provided by the counterjet detection, and the zone resolved with millimeter continuum interferometry (Piétu et al. 2006). The NIR scattered-light data suggest elongation in the E-W direction rather than along the system semi-major axis at P.A. = 147°/327° (Piétu et al. 2007). The F160W flux density of the disk from 0″3 < r < 0″8 is 18.1 mJy, at the faint end of the coronagraphically detected disks. Using our coronagraphic scale factor and the well-established H magnitude of GL 693, the scattering fraction for the MWC 480 disk at the epoch of the 1998 NICMOS observation is 0.437%. While the NICMOS PSF-subtracted imagery suggests some azimuthal asymmetry in the scattered-light data, the small angular range over which the disk is detected, together with color-mismatch errors in our PSF-subtracted data preclude measurement, except as a disk av-erage, prior to deprojection. The azimuthally averaged, but still projected, radial surface brightness profile is well fitted by an $r^{-5.1}$ power law from 0″3 to 0″8 (39 AU–105 AU; Figure 3(b)). Given the color mismatch between MWC 480 and GL 693, the angular range over which we detect the disk and the disk surface brightness is likely both underestimated.

Sitko et al. (2008) fitted the IR SED of MWC 480 using the Whitney et al. (2003a, 2003b, 2004) Monte Carlo Radiative Transfer (WMCRT) code. Adopting the inclination derived from millimeter imaging (Piétu et al. 2007) and a scattered-light disk outer radius of 2″2 (360 AU), they predict a disk radial surface brightness profile SB $\propto r^{-3.1}$, at 1.6 μm. This radial surface brightness profile is close to the value expected for a disk viewed at grazing illumination (e.g., "geometrically flat" in the terminology of Whitney & Hartmann 1992).

3.7.1. The Disk in Time

The detection of mid-IR photometric variability similar to HD 163296 prompted Sitko et al. (2008) to suggest that, like HD 163296 (Wisniewski et al. 2008), the disk of MWC 480 might be variably illuminated, with scattered-light imagery showing apparently variable disk structure. The *HST* data, both the NICMOS F160W detection and the STIS marginal detection, are consistent with variable illumination of the outer disk. For a variably illuminated disk, enhanced shadowing is expected as the inner disk inflates in high-accretion/IR excess states, while the outer disk is expected to be better illuminated in low-accretion states. The 1998 NICMOS observation was obtained within three days of an *ISO* SWS spectrum which Sitko et al. (2008) showed corresponded to a low IR excess state (Figure 10). There are no contemporary IR data at the epoch of the STIS observation. The 2004 NICMOS observation was obtained in a high IR excess state. Three months earlier, the star was observed with BASS, and was also in a high IR excess state, so it is likely that the 2004 October *FUSE* spectra were also obtained in a high-accretion state.
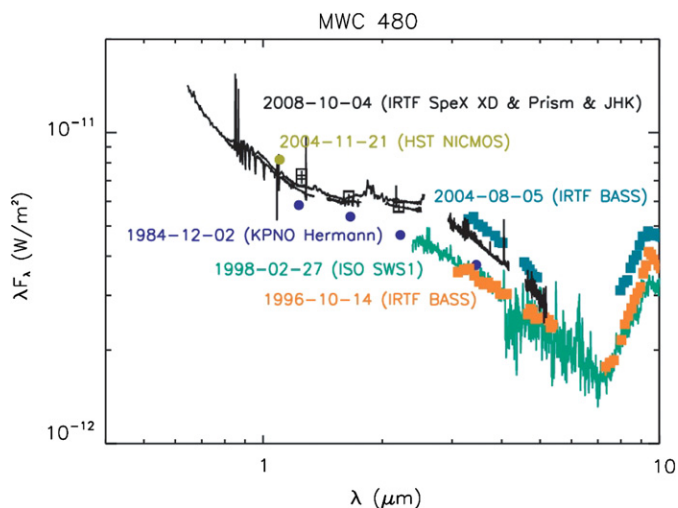

Figure 10. IR variability of MWC 480 since 2006. IR data obtained from 2006 to 2009 span the same range in IR excess noted by Sitko et al. (2008). For reference, the *ISO* SWS spectrum obtained within three days of the 1998 NICMOS coronagraphic image is shown, together with the 2004 high IR excess state data discussed in Sitko et al. (2008). Aperture photometry of a NICMOS F110W direct image obtained in tandem with the coronagraphic observation in 2004 November demonstrates that the NICMOS F110W imagery was also obtained in a high IR excess state.

3.7.2. Disk Stratification

Settling of the dust toward the disk midplane is an expected consequence of dust grain growth, while gas disks are not expected to settle (Dullemond & Dominik 2004a, 2004b), merely to disperse due to the effects of any wide-angle stellar wind, or to photoevaporate due to the EUV and FUV radiation field of the star. Thus, over time, protoplanetary disks are expected to become stratified, with the dust confined closer to the disk midplane than the gas (Brittain et al. 2007). The combination of gas data from the literature, the coronagraphic imagery, and SED data for MWC 480 allow us to explore this effect. The 10 ± 1.1 AU CO gas scale height at 100 AU (Piétu et al. 2007) corresponds to a disk opening half-angle of 6°. We can place limits on the dust disk opening half-angle by using the scale height for the inner rim of the dust disk at the dust sublimation radius of 0.3 AU for the SEDs discussed by Sitko et al. (2008). For the high IR excess/accretion state (2004) SED, shadowing of the entire outer disk occurs for disk opening half-angles ⩽3°0. The low IR excess/accretion SED, corresponding to the 1998 NICMOS data, places more stringent limits on shadowing of the dust disk: shadowing occurs for opening half-angles ⩽2°2. *HST* coronagraphic non-detections of the outer disk would be expected in the high IR state if the dust disk scale height is ⩽50% and in the low accretion state ⩽37% of the gas scale height. The NICMOS data suggest that the dust disk does not extend much above the 2°2 half-angle which would result in shadowing, providing a direct confirmation of the interpretation of the IR SED originally proposed by Meeus et al. (2001). Moreover, the smaller vertical extent of the dust disk compared to the gas disk, and the small opening half-angle for the gas disk indicate that the disk of MWC 480 is not only close to being geometrically flat, approaching values expected for debris disks which are not dynamically stirred by the presence of larger bodies in the disk (Thébault 2009), but is stratified. Most importantly for our purposes, such a geometrically flat disk should provide negligible extinction or foreground absorption toward the star at a viewing inclination

of 37°.5 from pole-on. Collectively these data are consistent with the optical extinction, $N(H_2)$ and $N(H\,\textsc{i})$ measured at Lyα arising from foreground interstellar material.

4. DISCUSSION

Of the lightly reddened Herbig Ae stars with moderate-quality CCD-resolution X-ray spectra, MWC 480 has the lowest current accretion and mass-loss rates, but the highest $N_{X\text{-ray}}(H)$. Line of sight measures of $E(B - V)$, $N(H\,\textsc{i})$, and $N(H_2)$ exclude the bulk of this absorption being due to foreground material, while the well-established viewing inclination of 37°.5 and both the flatness and stratification of the disk exclude the bulk of the absorption occurring in the circumstellar disk at $r \geqslant 0.3$ AU. The remaining option is for the photoelectric absorption to arise interior to the dust sublimation radius. As noted by Güdel et al. (2007), this region includes the basal portions of any jet component launched from the star, any wide-angle wind, and the zone where material accretes onto the star.

4.1. Excluding Photoelectric Absorption from a Jet or Wind

Assuming that the mass loss via a jet or wind correlates with accretion, as has been independently shown for HD 163296 (Wassell et al. 2006), we would expect photoelectric absorption associated with either a wide-angle wind or a jet to correlate with accretion rate or with FUV excess light. Our measurement of MWC 480's jet inclination and its agreement with the disk inclination demonstrates that the jet is perpendicular to the disk. If this is typical of other Herbig Ae star outflows, then photoelectric absorption due to jets should be most directly observable at low inclinations. Both AB Aur and HD 104237 have larger FUV excess luminosities and higher accretion rates than MWC 480 (Garcia Lopez et al. 2006; Donehew & Brittain 2010). While the jet from AB Aur has yet to be firmly detected in imagery, the star drives an extremely strong stellar wind (Bouret et al. 1997) producing high-velocity absorption seen in UV spectra. HD 104237 drives a bipolar jet, which has been imaged in Lyα (Grady et al. 2004). Both stars have favorable inclinations, close to pole-on, for detection of wind and/or jet material, yet neither star has $N(H)_{X\text{-ray}}$ significantly elevated above optical or UV estimates of $N(H)$. Similarly, higher inclination Herbig Ae stars, such as HD 163296, also have $N(H)$ consistent with (low) foreground extinction and $N(H)$ (Figure 11). $N(H)$ consistent with the line-of-sight dust column is also found for IRAS 04158+2805 (Glauser et al. 2008), where the gas-to-dust ratio is within a factor of 2 of the value typically assumed for the ISM. Collectively these data exclude an association with mass loss for the elevated photoelectric absorption.

4.2. Association with Accreting Material

If winds and jets are not responsible for producing the level of absorption seen in the *Chandra* data for MWC 480, the remaining location for producing $N_{X\text{-ray}}(H) = 5.2 \times 10^{21}$ cm^{-2} in a dust-free region is in association with accreting material. For T Tauri stars, funneled accretion is typically considered (e.g., DG Tau A; Güdel et al. 2007), and further discussed by Gregory et al. (2007) to reduce L_X for classical T Tauri stars compared to non-accreting weak-line T Tauri stars. Furthermore, for an accretion rate near $10^{-8}\ M_\odot$ yr^{-1}, the accretion footprint should be localized near the photosphere (Robrade & Schmitt 2007). In their study, photoelectric absorption is expected if the filling factor of the footprint is at the low end of the range inferred for T Tauri stars, near 0.01.

4.3. Geometry of the Accreting Material

Broad and asymmetric emission profiles are characteristic of accreting T Tauri stars. More recently, the presence of such profiles has been used to indicate the presence of accretion onto brown dwarfs (Jayawardhana et al. 2003; Mohanty et al. 2003; Reiners 2009). Accreting plasma is believed to be progressively shocked as it approaches the stellar surface. Thus, high ionization species, such as O $\textsc{vi}$ ($T \sim 300,000$ K), offer some indication of where the accretion footprint is on the stellar disk. Accretion that is preferentially confined to the disk midplane should produce emission profiles similar to, but broader than emission from species originating farther out in the disk (e.g., CO, Blake & Boogert 2004), with FWHM reflecting the stellar $v \sin i$. Such emission would produce narrow emission profiles at low inclination, broadening at intermediate inclination, and then becoming double peaked at high inclination, as seen in the CO data. For MWC 480, the O $\textsc{vi}$ emission should resemble the cuspy O $\textsc{vi}$ profile of Altair (Redfield et al. 2002), but with a smaller FWHM and separation between the emission peaks. Cuspy profiles are not seen in any of the three *FUSE* spectra of MWC 480. For Altair, the X-ray emission is also confined to low stellar latitudes (Robrade & Schmitt 2009), with a pronounced rotational modulation. The MWC 480 *Chandra* observation is much shorter than the Altair observation, but lacks any indication of variability. The *FUSE* data demonstrate variation on timescales as short as 1.7 days, while the data integrated over the individual *FUSE* orbits suggest a marginal detection of variability on timescales as short as 0.5 days, but not the presence of a distinct eclipse. These data are too sparse for tomographic studies: longer duration observations are required to establish or exclude rotational modulation. The *FUSE* data set for Herbig Ae stars, however, includes a number of stars with well-measured inclinations and can be used to constrain the location of the accretion footprint for these stars as a group.

The visibility of broad (optical) emission profiles over a wide range in system inclination has been used to indicate that the accretion footprints on classical T Tauri stars are located at (unspecified) "high" latitude (Hartigan et al. 1995; Fischer et al. 2008). Broad O $\textsc{vi}$ emission profiles are found in the spectra of Herbig Ae stars viewed at inclinations spanning $18 \leqslant i \leqslant 65°$ (Figure 11). At higher inclinations (e.g., HD 142666), circumstellar H$_2$ absorption becomes sufficiently strong that, while O $\textsc{vi}$ can be detected, the emission profile cannot be reconstructed. FUV excess light detections are firmly established for $i = 18°$ (HD 104237 A) through 50° (HD 163296). The FUSE Herbig Ae star data show no correlation between O $\textsc{vi}$ profile shape, FWHM, and system inclination (Figure 11). The *FUSE* data, therefore, *exclude* confinement of the O $\textsc{vi}$ emission close to the plane of the disk not only for MWC 480, but for the low-extinction Herbig Ae stars as a group.

The routine detectability of O $\textsc{vi}$ emission in MWC 480 and other actively accreting Herbig Ae stars further suggest that the bulk of the O $\textsc{vi}$ emitting region cannot be confined to a geometrically small spot at latitudes where the portions of the photosphere are occulted by stellar rotation, since we would have expected to have at least one non-detection among the *FUSE* observations. The *FUSE* data, however, are sufficiently sparse that we cannot distinguish between emission in a ring at moderate latitudes or an accretion spot with some fraction of its surface (say, 50% for MWC 480) extending into latitudes which are always visible (for MWC 480, $\geqslant 53°$). The photoelectric absorption data exclude the accretion footprint lying at exclusively polar latitudes, since then the elevated absorption would
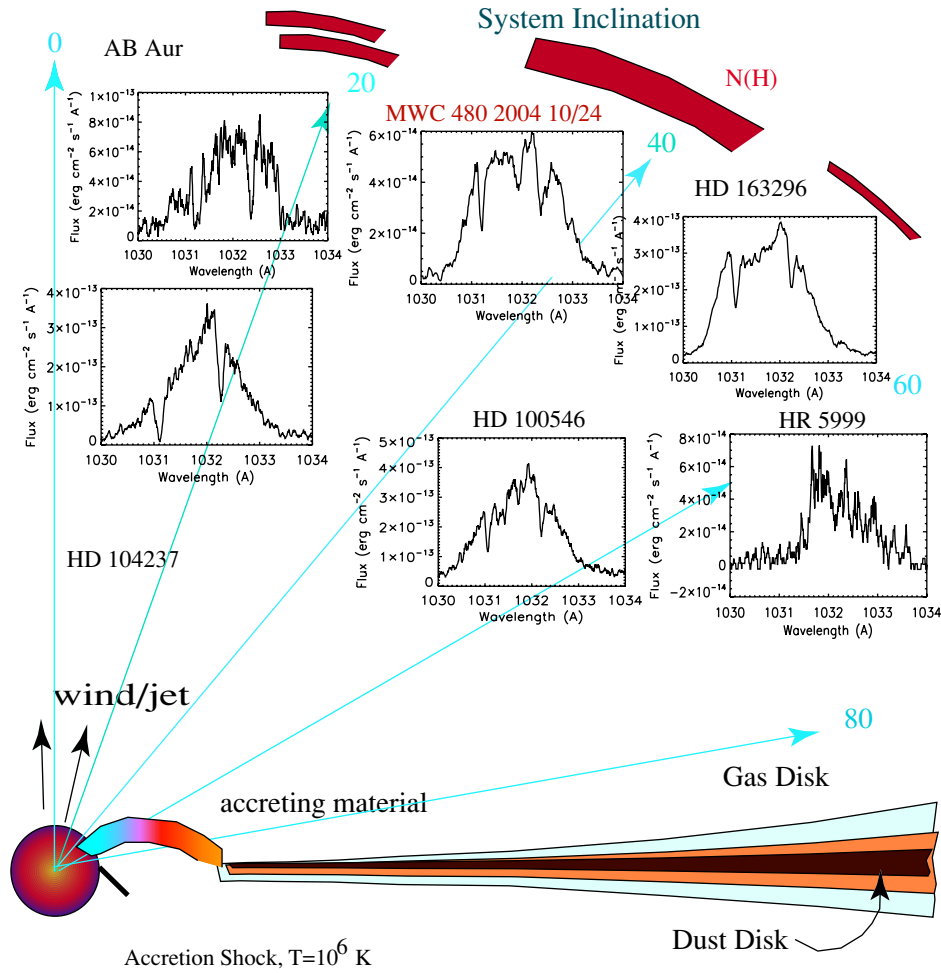
Figure 11. Broad O VI emission profiles are observed for the Herbig Ae stars with measured inclinations from $18 \leqslant i \leqslant 65°$. O VI 1032 Å profiles are shown for AB Aur (P2190301), HD 104237 (P1630202), HD 163296 (P2190601), HR 5999 (P1860201), HD 100546 (P2190401), and MWC 480 (E5100101 from 2004 October 24). The distribution of $N_{\text{X-ray}}(\text{H})$ in inclination is shown schematically as red bars. The gas disk of MWC 480 has an opening half-angle of $6°$, and a dust disk with half-angle $2°.2 \leqslant \theta \leqslant 3°.7$. The presence of an essentially geometrically flat dust and gas disk, coupled with the O VI and $N_{\text{X-ray}}(\text{H})$ data, exclude an origin for the elevated photoelectric absorption in a polar or wide angle wind. The remaining option is an origin in accreting material which is further constrained to be preferentially observed at high-temperate latitudes, similar to classical T Tauri stars such as DG Tau A.

be preferentially detected in low-inclination systems such as AB Aur and HD 104237, rather than in the intermediate-inclination MWC 480. The combination of the FUV and X-ray data for MWC 480 and other Herbig Ae stars favors the accretion footprint lying at high-temperate latitudes on the star, as has recently been found for some classical T Tauri stars (Güdel et al. 2007). Future, coordinated X-ray and FUV synoptic studies could more precisely localize the emission, and distinguish between spot(s) and an accretion ring, placing constraints on the magnetic field geometry for the star (Romanova et al. 2009).

4.4. Constraining the Magnetic Field

Independent of the exact geometry of the accretion footprint, lifting the accreting material from the disk midplane to moderate to high latitudes near the stellar photosphere *requires* coupling between the accreting plasma and a stellar magnetic field. For classical T Tauri stars, the field component with accretion for classical T Tauri stars earlier than mid-M in spectral type is a dipole component of the typically kilo-Gauss-strength, multipole field. Measured longitudinal field strengths for Herbig Ae stars similar to MWC 480 are small: typically $\sim$100 G (Wade

et al. 2007; Alecian et al. 2008; Hubrig et al. 2009; Wade et al. 2009). It is not clear how this translates into the average magnetic field strength over the surface of the star. We can place limits on the field strength, however, if we assume that the star is accreting magnetospherically. For magnetospheric accretion, the disk is truncated at a radius R_T, measured in stellar radii (2.1 $R_\odot$ for a star like MWC 480),

$$R_T = 7.1 B^{4/7} * \dot{M}^{-2/7} * M^{-1/7} * R^{5/7}. \tag{1}$$

The truncation radius depends upon the average surface magnetic field strength B in units of kG, the mass accretion rate $\dot{M}$ in units of $10^{-8} M_\odot \text{yr}^{-1}$, the stellar mass M in units of 0.5 $M_\odot$, and the stellar radius R in units of 2 $R_\odot$, following Bouvier et al. (2007). Our accretion rate estimates range from $\sim 3 \times 10^{-8}$ to $1.2 \times 10^{-7} M_\odot \text{yr}^{-1}$: for this calculation we adopt $(9 \pm 3) \times 10^{-8} M_\odot \text{yr}^{-1}$. We further assume that the CO emission extends into the truncation radius. Blake & Boogert (2004) find a half-width at zero intensity (HWZI) for the CO fundamental emission at $100 \pm 10 \text{km s}^{-1}$, which corresponds to 0.07 $\pm$ 0.03 AU. This implies that the average surface field strength is $B_{\text{avg}} = 3^{+5}_{-2}$ kG. This is a large range, but is comparable to

field strengths reported for classical T Tauri stars (Valenti & Johns-Krull 2004, e.g., 1–6 kG with an average of 2.2 kG), and would clearly be sufficient to enable accretion processes closely resembling those operating on classical T Tauri stars. With an estimated age of 7 Myr (Simon et al. 2000), the data for MWC 480 suggest that such fields can remain significant for much of the first 10 Myr of an intermediate-mass star's life. Measurement of a stronger longitudinal magnetic field for the lower accretion rate Herbig Ae star HD 139614 compared with MWC 480 further indicates that the end of accretion onto intermediate-mass PMS stars cannot be solely due to fading of the stellar magnetic field. Moreover, the continued presence of a gas-rich, but otherwise stratified disk in an older 1.7 $M_\odot$ Herbig Ae star suggests that the cumulative FUV and EUV radiation dose experienced by the disk over 7 Myr is insufficient to clear the inner disk via photo-evaporation, but may be responsible for the small CO scale height compared to disks around T Tauri stars. Additional processes, potentially including dynamical clearing by giant planet formation, must also be involved in disk clearing and the production of transitional disks among Herbig Ae stars. In the case of MWC 480, however, the continued presence of a gas-rich disk and disk–star coupling similar to that of (typically younger) classical T Tauri stars suggests that Jovian-mass bodies have yet to form around this star.

5. SUMMARY

In this pan-chromatic study, we demonstrate that the Herbig Ae star MWC 480 is actively accreting, with a first detection of X-ray emission from the star, and an FUV detection of excess continuum light typical of accreting PMS stars, together with broad emission lines. Accretion signatures are also seen in the Balmer jump and at Br γ. The available data suggest an accretion rate of a few $\times 10^{-8}\ M_\odot\ \mathrm{yr}^{-1}$. The star also drives a bipolar jet, which while optically detected, is not seen in the X-ray in our short *Chandra* observation. Unexpectedly for a star that is detected in the FUV, the X-ray data for MWC 480 demonstrate soft X-ray photoelectric absorption at a level $\sim 10\times$ that expected based on line-of-sight measures of $N(\mathrm{H}_2)$, $E(B-V)$, and limits on $N(\mathrm{H\ I})$.

In a re-analysis of archival *HST* coronagraphic imagery, we detect the disk in scattered light at $1.6\ \mu\mathrm{m}$, with low surface brightness and morphology consistent with the disk being illuminated at grazing incidence. This detection was obtained at an epoch when the near-IR excess was at minimum light, suggesting that the disk is geometrically flat. We compare the disk opening half-angle for the gas, obtained from the literature, with estimates for the half-angle required to plunge the outer disk into shadow at IR minimum light, and conclude that the disk is not only close to being geometrically flat, but is stratified, with a dust scale height only 37% that of the gas. When viewed at an inclination of 37°.5 from pole-on, such a disk will produce negligible extinction, or molecular gas absorption, suggesting that the line-of-sight material has a foreground, interstellar origin, consistent with the $N(\mathrm{HD})/N(\mathrm{H}_2)$ ratio.

We next consider production of the photoelectric absorption interior to the dust sublimation radius, and evaluate a wind and/or jet origin or an accretion origin for the absorption. A wind or jet origin is excluded since photoelectric absorption should correlate with mass-loss rate, and be preferentially observed in systems viewed close to pole-on: such behavior is not seen in the Herbig Ae stars with good inclination data. This leaves an accretion origin for the photoelectric absorption, and for the O VI emission seen in the FUV. Broad O VI emission in Herbig Ae

stars is found for inclinations from pole-on through at least 65°, without the correlation of profile shape with inclination expected for a species confined to the disk midplane or a low latitude belt on the star, excluding equatorially concentrated accretion for Herbig Ae stars. Detection of enhanced photoelectric absorption in the line of sight to MWC 480 and not toward other Herbig Ae stars further suggests that the accretion footprint is located at high-temperate latitudes on the star, similar to the geometry inferred for the classical T Tauri star DG Tau A (Güdel et al. 2007). Demonstrating that this latitude dependence is typical of intermediate-mass PMS stars will require X-ray observations of other moderate inclination of Herbig Ae stars. However, the presence of non-equatorial accretion onto Herbig Ae stars indicates that, as for classical T Tauri stars, a stellar magnetic field is required to lift plasma from the disk midplane to high-temperate latitudes on the star.

REFERENCES

Alecian, E., et al. 2008, arXiv:0809.4286
Augereau, J.-C., Lagrange, A. M., Mouillet, D., & Ménard, F. 2001, A&A, 365, 78

Beskrovnaya, N. G., & Pogodin, M. A. 2004, A&A, 414, 955
Blake, G. A., & Boogert, A. C. A. 2004, ApJ, 606, L73
Blondel, P. F. C., & Tjin A Djie, H. R. E. 2006, A&A, 456, 1045
Bouret, J.-C., Catala, C., & Simon, T. 1997, A&A, 328, 606
Bouvier, J., Alencar, S. H. P., Harries, T. J., Johns-Krull, C. M., & Romanova,
    M. M. 2007, Protostars and Planets V, ed. B. Reipurth, D. Jewitt, & K. Keil
    (Tucson, AZ: Univ. Arizona Press), 479
Brittain, S. D., Simon, T., Najita, J. R., & Rettig, T. W. 2007, ApJ, 659, 685
Calvet, N., & Gullbring, E. 1998, ApJ, 509, 802
Calvet, N., Muzerolle, J., Briceño, C., Hernández, J., Hartmann, L., Saucedo, J.
    L., & Gordon, K. D. 2004, AJ, 128, 1294
Collins, K. A., et al. 2009, ApJ, 697, 557
Cushing, M. C., Vacca, W. D., & Rayner, J. T. 2004, PASP, 116, 362
Cutri, R. M., et al. 2003, Explanatory Supplement to the 2MASS All Sky Data
    Release (Washington: NASA), http://www.ipac.caltech.edu/2mass/releases/
    allsky/doc/explsup.html
Devine, D., Grady, C. A., Kimble, R. A., Woodgate, B., Bruhweiler, F. C.,
    Boggess, A., Linsky, J. L., & Clampin, M. 2000, ApJ, 540, L57
Dixon, W. V., et al. 2007, PASP, 119, 527
Donati, J.-F., et al. 2008, MNRAS, 386, 1234
Donati, J.-F, et al. 2010, MNRAS, 403, 159
Donehew, B., & Brittain, S. 2010, ApJ, submitted
Dullemond, C. P. E., & Dominik, C. 2004a, A&A, 417, 159
Dullemond, C. P. E., & Dominik, C. 2004b, A&A, 421, 1075
Feigelson, E., Lawson, W. A., & Garmire, G. P. 2003, ApJ, 599, 1207
Fischer, W., Kwan, J., Edwards, S., & Hillenbrand, L. 2008, ApJ, 687, 1117
Garcia Lopez, R., Natta, A., Testi, L., & Habart, E. 2006, A&A, 459, 837
Garmire, G. P., Bautz, M. W., Ford, P. G., Nousek, J. A., & Ricker, G. R., Jr.
    2003, Proc. SPIE, 4851, 28
Garrison, L. M., Jr. 1978, ApJ, 224, 535
Glauser, A. M., Ménard, F., Pinte, C., Duchêne, G., Güdel, M., Monin, J.-L., &
    Padgett, D. L. 2008, A&A, 485, 531
Grady, C. A., et al. 2004, ApJ, 608, 809
Grady, C. A., et al. 2005, ApJ, 630, 958
Grady, C. A., et al. 2007, ApJ, 665, 1391
Gregory, S. G., Wood, K., & Jardine, M. M. 2007, MNRAS, 379, L35
Grosso, N., Bouvier, J., Montmerle, T., Fernández, M., Grankin, K., & Zapatero
    Osorio, M. R. 2007, A&A, 475, 607
Güdel, M., Telleschi, A., Audard, M., Skinner, S. L., Briggs, K. R., Palla, F., &
    Dougados, C. 2007, A&A, 468, 515
Günther, H. M., & Schmitt, J. H. M. M. 2009, A&A, 494, 1041
Hackwell, J. H., et al. 1990, Proc. SPIE, 1235, 171
Hamaguchi, K., Yamauchi, S., & Koyama, K. 2005, ApJ, 618, 360
Hartigan, P., Edwards, S., & Ghandour, L. 1995, ApJ, 452, 736
Hubrig, S., et al. 2009, A&A, 502, 283
Hughes, A. M., Wilner, D. J., Qi, C., & Hogerheijde, M. R. 2008, ApJ, 678,
    1119
Jayawardhana, R., Mohanty, S., & Basri, G. 2003, ApJ, 592, 282
Kozlova, O. V., Alekseev, I. Yu., & Shakhovskoi, D. N. 2007, Astrophysics, 50,
    467
Leggett, S. K., et al. 2006, MNRAS, 373, 381
Lowrance, P. J., et al. 1999, ApJ, 512, L69
Mannings, V., Koerner, D., & Sargent, A. I. 1997, Nature, 388, 555
Martin-Zaïdi, C., et al. 2008, A&A, 484, 225
Meeus, G., Waters, L. B. F. M., Bouwman, J., van den Ancker, M. E., Waelkens,
    C., & Malfait, K. 2001, A&A, 365, 476
Mohanty, S., Jayawardhana, R., & Barrado y Navascués, D. 2003, ApJ, 593,
    L109
Monet, D. G., et al. 2003, AJ, 125, 984
Moos, H. W., et al. 2000, ApJ, 538, L1
Muzerolle, J., D'Alessio, P., Calvet, N., & Hartmann, L. 2004, ApJ, 617, 406
Muzerolle, J., Hartmann, L., & Calvet, N. 1998, AJ, 116, 2965

Piétu, V., Dutrey, A., & Guilloteau, S. 2007, A&A, 488, 565
Piétu, V., Dutrey, A., Guilloteau, S., Chapillon, E., & Pety, J. 2006, A&A, 460,
    L43
Rayner, J. T., et al. 2003, PASP, 115, 362
Redfield, S., Linsky, J. L., Ake, T. B., Ayres, T. R., Dupree, A. K., Robinson, R.
    D., Wood, B. E., & Young, P. R. 2002, ApJ, 581, 626
Reiners, A. 2009, ApJ, 702, L119
Roberge, A., et al. 2001, ApJ, 551, L97
Robrade, J., & Schmitt, J. H. M. M. 2007, A&A, 473, 229
Robrade, J., & Schmitt, J. H. M. M. 2009, A&A, 497, 511
Romanova, M. M., Long, M., Lamb, F. K., Kulkarni, A. K., & Donati, J.-F.
    2009, MNRAS, submitted (arXiv:0912.1681)
Ryter, Ch. 1996, Ap&SS, 236, 285
Sasseen, T. P., Hurwitz, M., Dixon, W. V., & Airleau, S. 2002, ApJ, 566, 267
Schneider, G., Silverstone, M. D., & HInes, D. 2005, ApJ, 629, L117
Simon, M., Dutrey, A., & Guilloteau, S. 2000, ApJ, 545, 1034
Simons, D. A., & Tokunaga, A. 2002, PASP, 114, 169
Sitko, M. L., Meade, M. R., & Savage, B. D. 1981, ApJ, 246, 161
Sitko, M. L., et al. 2008, ApJ, 678, 1070
Skinner, S. L., Güdel, M., Audard, M., & Smith, K. 2004, ApJ, 614, 221
Skrutskie, M. F., et al. 2006, AJ, 131, 1163
Sloan, G. C., Kraemer, K. E., Price, S. D., & Shipman, R. F. 2003, ApJS, 147,
    379
Snow, T. P., Ross, T. L., Destree, J. D., Drosback, M. M., Jensen, A. G., Rachford,
    B. L., Sonnentrucker, P., & Ferlet, R. 2008, ApJ, 688, 1124
Stecklum, B., Melnikov, S. Y., & Meusinger, H. 2007, A&A, 463, 621
Stelzer, B., Micela, G., Hamaguchi, K., & Schmitt, J. H. M. M. 2006, A&A,
    457, 223
Stelzer, B., Robrade, J., Schmitt, J. H. M. M., & Bouvier, J. 2009, A&A, 493,
    1109
Swartz, D. A., Drake, J. L., Elsner, R. F., Ghosh, K. K., Grady, C. A., Wassell,
    E., Woodgate, B. E., & Kimble, R. A. 2005, ApJ, 628, 811
Telleschi, A., Güdel, M., Briggs, K. R., Skinner, S. L., Audard, M., &
    Franciosini, E. 2007, A&A, 468, 541
Testa, P., Huenemoerder, D. P., Schultz, N. S., & Ishibashi, K. 2008, ApJ, 687,
    579
Thébault, P. 2009, A&A, 505, 1269
Tokunaga, A. T., Simons, D. A., & Vacca, W. D. 2002, PASP, 114, 180
Tokunaga, A. T., & Vacca, W. D. 2005, PASP, 117, 421
Tsuboi, Y., Maeda, Y., Feigelson, E. D., Garmire, G. P., Chartas, G., Mori, K.,
    & Pravdo, S. H. 2003, ApJ, 587, L51
Vacca, W. D., Cushing, M. C., & Rayner, J. T. 2003, PASP, 115, 389
Valenti, J. A., & Johns-Krull, C. M. 2004, Ap&SS, 292, 619
van den Ancker, M. E., de Winter, D., & Tjin A Djie, H. R. E. 1998, A&A, 330,
    145
Wade, G. A., Alecian, E., Grunhut, J., Catala, C., Bagnulo, S., Folsom, C. P., &
    Landstreet, J. D. 2009, arXiv:0901.0347
Wade, G. A., Bagnulo, S., Drouin, D., Landstreet, J. D., & Monin, D.
    2007, MNRAS, 376, 1145
Wassell, E. J., Grady, C. A., Woodgate, B., Kimble, R. A., & Bruhweiler, F. C.
    2006, ApJ, 650, 985
Whitney, B. A., & Hartmann, L. 1992, ApJ, 395, 529
Whitney, B. A., Indebetouw, R., Bjorkman, J. E., & Wood, K. 2004, ApJ, 617,
    1177
Whitney, B. A., Wood, K., Bjorkman, J. E., & Cohen, M. 2003a, ApJ, 598,
    1079
Whitney, B. A., Wood, K., Bjorkman, J. E., & Wolff, M. J. 2003b, ApJ, 591,
    1049
Williger, G. M., Oliveira, C., Hébrand, G., Dupuis, J., Dreizler, S., & Moos,
    W. M. 2005, ApJ, 625, 210
Wisniewski, J. P., Clampin, M., Grady, C. A., Ardila, D. R., Ford, H. C.,
    Golimowski, D. A., Illingworth, G. D., & Krist, J. E. 2008, ApJ, 82, 548